Model updating for a large multi-span quasi-periodic viaduct based on free wave characteristics[⋆,⋆⋆]

Jie Zhang[a,*], Kristof Maes[a], Guido De Roeck[a], Geert Lombaert[a,**]

[a] *KU Leuven, Department of Civil Engineering, Leuven, Belgium*

Abstract

Quasi-periodic structures, as found in multi-span bridges, multi-bay and multi-storey buildings, are often characterized by a high modal density, even at low frequencies. This clustering of modes poses challenges in operational modal analysis, as well as in finite element model updating, where a pairing of experimental and numerically predicted modes is required. To overcome these difficulties, an alternative method for model updating based on the so-called free wave characteristics has recently been proposed. In this work, this method is applied to calibrate a finite element model of the K032 viaduct of the A11 highway in Bruges, Belgium. Vibration measurements are conducted to experimentally determine the free wave characteristics of the viaduct. In the model updating, the discrepancy between the calculated and identified free wave characteristics is minimized. The results are validated by comparing measured frequency response functions with those obtained from the updated finite element model.

Keywords: structural dynamics, model updating, periodic structures, free wave characteristics, free wave identification, multi-span viaduct

1. Introduction

Vibration-based finite element model updating is widely used in civil engineering to calibrate numerical models with poorly known parameters [1, 2, 3]. The model updating is usually performed by minimizing the discrepancy between calculated and experimentally identified dynamic data, which generally consist of modal characteristics, including natural frequencies and mode shapes. For repetitive structures, as often found in multi-span bridges and multi-bay and multi-storey buildings, such as parkings and office buildings, mode clustering tends to occur, resulting in closely-spaced natural frequencies characterized by mode shapes with similar wavelength [4, 5]. This makes it difficult to distinguish between these modes in operational modal analysis and consequently poses challenges in model updating, where the matching of measured and calculated modes is required.

⋆ *Postprint submitted to Journal of Sound and Vibration*

⋆⋆ *Published version:* J. Zhang, K. Maes, G. De Roeck, and G. Lombaert. Model updating for a large multi-span quasi-periodic viaduct based on free wave characteristics. *Journal of Sound and Vibration*, 506:116161, 2021. `https://doi.org/10.1016/j.jsv.2021.116161`

* Presently employed at Siemens Industry Software NV, Leuven, Belgium.

** Corresponding author. Tel.: +32 (0) 16 32 17 72.

Email address: `geert.lombaert@kuleuven.be` (Geert Lombaert)

As an alternative to model updating based on modal characteristics, the use of free wave characteristics in model updating of one-dimensional periodic structures has been explored in [5]. A one-dimensional periodic structure is composed of identical units that are connected side by side in an identical way [6]. The free wave characteristics of a periodic structure consist of propagation constants and corresponding free waves [7, 8]. As shown by Zhang et al. in [5], these characteristics serve as a valuable alternative for model updating of periodic and quasi-periodic structures.

In the work of Zhang et al. [5], a non-linear least-squares method is proposed to identify free wave characteristics from the measured response of a periodic structure, in extension of the method proposed by Junyi and Balint in [9]. The authors have also explored the use of free wave characteristics in model updating for a simple lab structure. Apart from circumventing the aforementioned challenges concerning mode distinction and mode matching, model updating based on free wave characteristics has the advantage that the measurement of a small number of (consecutive) repetitive units is sufficient, rather than requiring the covarage of the entire structure. In the present paper, the model updating technique proposed in [5] is applied to a finite element model of the K032 viaduct (Fig. 1), a large multi-span quasi-periodic viaduct in Bruges, Belgium. The free wave characteristics used in the model updating are identified from vibration measurements on the bridge deck. It is shown how the model updating leads to a better prediction of the free waves and frequency response functions which were identified from the in situ tests. The resulting model will therefore allow for a more accurate prediction of the dynamic response of the structure as built, which is useful for a validation of the design calculations as well as in case of modifications of the structure or design loads.

The paper is outlined as follows. Section 2 briefly recapitulates the methodology adopted in the model updating. Next, Section 3 presents the K032 viaduct and the measurement setup. Section 4 describes the results of the free wave identification. Section 5 presents the model updating based on free wave characteristics and discusses complementarity with other approaches. Finally, Section 6 concludes the work.

(a)  (b) 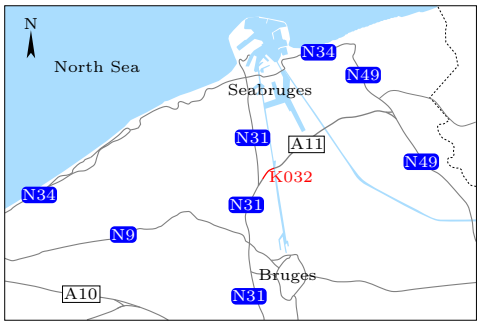

Fig. 1: (a) The K032 viaduct in Bruges, Belgium, and (b) situation sketch.

2. Methodology

Consider the case of an unbounded one-dimensional periodic structure. A conceptual example of such a structure as previously considered in [5] is shown in Fig. 2. As mentioned before, repetitive structures are characterized by mode clustering, which poses challenges in operational modal analysis and model updating. In this paper, the focus is on the use of identified free wave characteristics as an alternative of using identified modal characteristics in model updating for periodic structures.

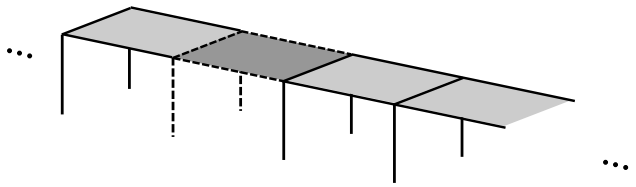

Fig. 2: Conceptual model of an infinite repetitive frame structure with plates (areas), beams and columns (lines). The repetitive unit is indicated with dashed lines.

This section summarizes the main aspects of the procedure presented in [5] for model updating based on identified free wave characteristics. First, subsection 2.1 explains how the free wave characteristics are calculated based on a finite element model of the structure. Next, subsection 2.2 presents the procedure followed for identifying the free wave characteristics of a structure based on in situ response measurements. Finally, subsection 2.3 explains how the calculated and identified free wave characteristics are combined in a model updating.

2.1. The calculation of free wave characteristics

The calculation of free wave characteristics is briefly recapitulated for the case of multi-coupled one-dimensional infinite periodic structures, following Mead [8]. The free wave characteristics of a periodic structure can be computed by analyzing a single repetitive unit cell. For the conceptual structure shown in Fig. 2, a potential model of the repetitive unit is shown in Fig. 3. The degrees of freedom in the model are separated in n_c so-called coupling degrees of freedom, at the left, respectively right interface with the adjacent units, Γ_L and Γ_R, and $n_\mathrm{dof} - n_\mathrm{c}$ internal degrees of freedom, with n_dof the total number of degrees of freedom in the model of the unit cell.

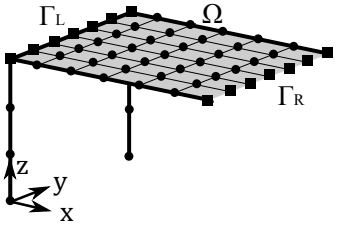

Fig. 3: Repetitive unit cell with interface nodes (squares) and internal nodes (circles).

In general, the forces at the two interfaces of the unit cell, $\hat{\mathbf{F}}_\mathrm{L}(\omega)$ and $\hat{\mathbf{F}}_\mathrm{R}(\omega)$ for a given frequency ω are related to the displacements at the two interfaces, $\hat{\mathbf{u}}_\mathrm{L}(\omega)$ and $\hat{\mathbf{u}}_\mathrm{R}(\omega)$ as follows:

$$\begin{bmatrix}\hat{\mathbf{F}}_\mathrm{L}(\omega)\\ \hat{\mathbf{F}}_\mathrm{R}(\omega)\end{bmatrix} = \begin{bmatrix}\mathbf{D}^{(\mathrm{c})}_{\mathrm{LL}}(\omega) & \mathbf{D}^{(\mathrm{c})}_{\mathrm{LR}}(\omega)\\ \mathbf{D}^{(\mathrm{c})}_{\mathrm{RL}}(\omega) & \mathbf{D}^{(\mathrm{c})}_{\mathrm{RR}}(\omega)\end{bmatrix} \begin{bmatrix}\hat{\mathbf{u}}_\mathrm{L}(\omega)\\ \hat{\mathbf{u}}_\mathrm{R}(\omega)\end{bmatrix} \tag{1}$$

where $\mathbf{D}^{(\mathrm{c})}_{\alpha\beta}(\omega)$ is the condensed dynamic stiffness matrix relating the forces applied to the set α of degrees of freedom to the displacements at the set β of degrees of freedom. For the sake of convenience, the frequency is omitted as an argument in the following.

Following the Floquet theory [7, 8], the interface forces and displacements at one unit cell r are related to those of the next unit cell $r+1$ as follows:

$$\hat{\mathbf{u}}_{\mathrm{L},r+1} = e^{\mu}\hat{\mathbf{u}}_{\mathrm{L},r} \tag{2}$$

$$\hat{\mathbf{F}}_{\mathrm{L},r+1} = e^{\mu}\hat{\mathbf{F}}_{\mathrm{L},r} \tag{3}$$

where $\mu \in \mathbb{C}$ is the frequency-dependent propagation constant. The real and imaginary part of the propagation constant μ indicate respectively the attenuation and phase change of the corresponding wave across a unit cell. Please note that the imaginary part of the propagation constant μ is only determined up to a factor 2π, since $e^{\mu} = e^{\mu+2\pi i\beta}$ for any integer β. For the sake of convenience, we always choose $\mu \in [-\pi, \pi)$.

Compatibility of the displacements and equilibrium at the interfaces require the following equations to hold:

$$\hat{\mathbf{u}}_{\mathrm{L},r+1} = \hat{\mathbf{u}}_{\mathrm{R},r} \tag{4}$$

$$\hat{\mathbf{F}}_{\mathrm{L},r+1} = -\hat{\mathbf{F}}_{\mathrm{R},r} \tag{5}$$

Combination of Eqs. (1–5) yields the following generalized eigenvalue problem:

$$\left(\mathbf{D}^{(\mathrm{c})}_{\mathrm{LR}}e^{2\mu} + (\mathbf{D}^{(\mathrm{c})}_{\mathrm{LL}} + \mathbf{D}^{(\mathrm{c})}_{\mathrm{RR}})e^{\mu} + \mathbf{D}^{(\mathrm{c})}_{\mathrm{RL}}\right)\hat{\mathbf{u}}_{\mathrm{L}} = \mathbf{0} \tag{6}$$

By solving the eigenvalue problem in Eq. (6), n_{c} pairs of free waves are obtained, denoted as $[\mu_{\mathrm{p}k},\ \boldsymbol{\psi}_{\mathrm{p}k}]$ and $[\mu_{\mathrm{n}k},\ \boldsymbol{\psi}_{\mathrm{n}k}]$, respectively, where $\boldsymbol{\psi} \in \mathbb{C}^{n_{\mathrm{c}}\times 1}$ is the free wave displacement vector. Each pair of free waves contains one positive going ("p") and one negative going free wave ("n"). The propagation constants $\mu_{\mathrm{p}k}$ and $\mu_{\mathrm{n}k}$ are equal in magnitude but opposite in sign, i.e. $\mu_{\mathrm{p}k} = -\mu_{\mathrm{n}k}$ [10].

2.2. The identification of free wave characteristics

Consider the case where the vibration response of a structure consisting of n_{u} repetitive unit cells (Fig. 4) is measured, for example using accelerometers. The method adopted in this work assumes that the response is only measured at the interface between different unit cells and that the excitation is applied at one end, i.e. either at the left interface of unit cell 1 or at the right interface of unit cell n_{u}. Only the first option is elaborated in the following.

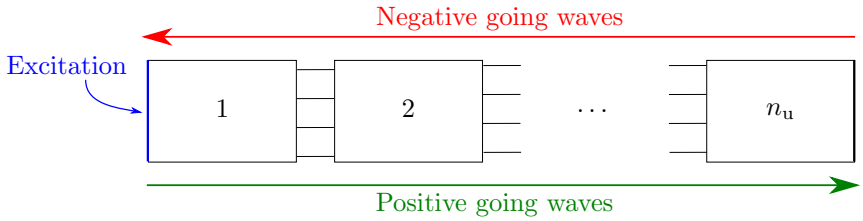

Fig. 4: Scheme of n_{u} repetitive unit cells with excitation at the left interface of unit cell 1, with an indication of the direction of the positive and negative going waves.

Following Mead [8], the forced vibration response in any unit cell r of a finite periodic structure excited at its ends (Fig. 4) is obtained by linear superposition of all characteristic free waves as follows:

$$\hat{\mathbf{u}}_{\mathrm{L},r} = \sum_{k=1}^{n_{\mathrm{c}}}(\lambda_{\mathrm{p}k}^{r-1}\boldsymbol{\psi}_{\mathrm{p}k}\alpha_{\mathrm{p}k} + \lambda_{\mathrm{n}k}^{-n_{\mathrm{u}}+r-1}\boldsymbol{\psi}_{\mathrm{n}k}\alpha_{\mathrm{n}k}) = \sum_{k=1}^{n_{\mathrm{c}}}(\lambda_{\mathrm{p}k}^{r-1}\boldsymbol{\psi}_{\mathrm{p}k}\alpha_{\mathrm{p}k} + \lambda_{\mathrm{p}k}^{n_{\mathrm{u}}-r+1}\boldsymbol{\psi}_{\mathrm{n}k}\alpha_{\mathrm{n}k}) \tag{7}$$

where $\lambda_{\mathrm{p}k}^{r-1}\boldsymbol{\psi}_{\mathrm{p}k}\alpha_{\mathrm{p}k}$ is the contribution of the kth positive going free wave and $\lambda_{\mathrm{n}k}^{-n_{\mathrm{u}}+r-1}\boldsymbol{\psi}_{\mathrm{n}k}\alpha_{\mathrm{n}k}$ is the contribution of the kth negative going freewave, with $\alpha_{\mathrm{p}k}$ and $\alpha_{\mathrm{n}k}$ the corresponding generalized coordinates and $\lambda_{\mathrm{p}k} = \mathrm{e}^{\mu_{\mathrm{p}k}}$, $\lambda_{\mathrm{n}k} = \mathrm{e}^{\mu_{\mathrm{n}k}}$, and $\lambda_{\mathrm{p}k} = \lambda_{\mathrm{n}k}^{-1}$.

Next, assume that the response of a given unit cell r is measured at a limited number n_{m} of interface degrees of freedom ($0 \leq n_{\mathrm{m}} \leq n_{\mathrm{c}}$), which are the same for every unit cell r, with $r = 1, \ldots, n_{\mathrm{u}}$. Under the additional assumption that only n_{w} pairs of free waves significantly contribute to the response at the considered frequency ω, the response $\hat{\mathbf{d}}_r \in \mathbb{C}^{n_{\mathrm{m}}\times 1}$ at the left side of unit cell r is given by:

$$\hat{\mathbf{d}}_r = \mathbf{L}\hat{\mathbf{u}}_{\mathrm{L},r} = \mathbf{L}\sum_{k=1}^{n_{\mathrm{w}}}(\lambda_{\mathrm{p}k}^{r-1}\boldsymbol{\psi}_{\mathrm{p}k}\alpha_{\mathrm{p}k} + \lambda_{\mathrm{p}k}^{n_{\mathrm{u}}-r+1}\boldsymbol{\psi}_{\mathrm{n}k}\alpha_{\mathrm{n}k}) = \sum_{k=1}^{n_{\mathrm{w}}}(\lambda_{\mathrm{p}k}^{r-1}\mathbf{x}_{\mathrm{p}k} + \lambda_{\mathrm{p}k}^{n_{\mathrm{u}}-r+1}\mathbf{x}_{\mathrm{n}k}) \tag{8}$$

where $\mathbf{L} \in \mathbb{R}^{n_{\mathrm{m}}\times n_{\mathrm{c}}}$ is a selection matrix that selects the n_{m} measured degrees of freedom from all n_{c} coupling degrees of freedom.

The free wave identification consists of estimating the eigenvalues $\lambda_{\mathrm{p}k} \in \mathbb{C}$ together with the free wave vectors $\mathbf{x}_{\mathrm{p}k} \in \mathbb{C}^{n_{\mathrm{m}}\times 1}$ and $\mathbf{x}_{\mathrm{n}k} \in \mathbb{C}^{n_{\mathrm{m}}\times 1}$, $k = 1, \ldots, n_{\mathrm{w}}$, from a set of data collected simultaneously at different unit cells $\hat{\mathbf{d}}_r$, with $r = 1, \ldots, n_{\mathrm{u}}$, when adopting an excitation at the left interface of unit cell 1 (Fig. 4). The data can be obtained directly from the measurements (displacement, strain, velocity or acceleration) or may alternatively consist of frequency response functions (FRFs) that are derived from combined force and response measurements. This is further addressed in Section 4.

Following Zhang et al. [5], the free wave characteristics $\lambda_{\mathrm{p}k}$, $\mathbf{x}_{\mathrm{p}k}$, and $\mathbf{x}_{\mathrm{n}k}$ can be obtained by solving the following least squares optimization problem:

$$[\lambda_{\mathrm{p}k};\ \mathbf{x}_{\mathrm{p}k};\ \mathbf{x}_{\mathrm{n}k}]^{\star} = \underset{[\lambda_{\mathrm{p}k};\ \mathbf{x}_{\mathrm{p}k};\ \mathbf{x}_{\mathrm{n}k}]}{\arg\min} \left\| \begin{bmatrix} \sum_{k=1}^{n_{\mathrm{w}}}(\mathbf{x}_{\mathrm{p}k} + \lambda_{\mathrm{p}k}^{n_{\mathrm{u}}}\mathbf{x}_{\mathrm{n}k}) \\ \sum_{k=1}^{n_{\mathrm{w}}}(\lambda_{\mathrm{p}k}\mathbf{x}_{\mathrm{p}k} + \lambda_{\mathrm{p}k}^{(n_{\mathrm{u}}-1)}\mathbf{x}_{\mathrm{n}k}) \\ \vdots \\ \sum_{k=1}^{n_{\mathrm{w}}}(\lambda_{\mathrm{p}k}^{n_{\mathrm{u}}}\mathbf{x}_{\mathrm{p}k} + \mathbf{x}_{\mathrm{n}k}) \end{bmatrix} - \begin{bmatrix} \mathbf{d}_1 \\ \mathbf{d}_2 \\ \vdots \\ \mathbf{d}_{n_{\mathrm{u}}+1} \end{bmatrix} \right\|_2^2 \tag{9}$$

For the case study presented in this work, the optimization problem in Eq. (9) is solved by means of the Levenberg Marquardt optimization algorithm implemented in the non-linear least-squares optimization routine (lsqnonlin) contained in MATLAB [11].

The number of free wave pairs n_{w} that significantly contributes to the response is generally not known a priori. To overcome this problem, it is proposed in [5] to solve the optimization problem in Eq. (9) for increasing values of n_{w} and afterwards adopting a stabilization diagram for the selection of stable and hence physical free waves [12]. This is also further addressed in Section 4.

The maximum number of free waves that can be identified depends on the sensor configuration. For a given frequency ω, the unknowns to be determined in the solution of Eq. (9) consist of n_{w} eigenvalues $\lambda_{\mathrm{p}k}$ and $n_{\mathrm{w}} \times 2n_{\mathrm{m}}$ components of the free wave vectors $\mathbf{x}_{\mathrm{p}k}$ and $\mathbf{x}_{\mathrm{n}k}$, i.e. $n_{\mathrm{w}}(1 + 2n_{\mathrm{m}})$ unknowns in total. The number of equations in the optimization problem equals the total number of response measurements within the zone of repetitive units, i.e. $(n_{\mathrm{u}}+1)n_{\mathrm{m}}$. For a unique solution of the least squares optimization problem in Eq. (9), the number of equations should be larger than or equal to the number unknowns, which yields the following upper limit for the number of free wave pairs that can be identified for a given sensor configuration:

$$n_{\mathrm{w}} \leq \frac{(n_{\mathrm{u}} + 1)n_{\mathrm{m}}}{(1 + 2n_{\mathrm{m}})} \tag{10}$$

2.3. Model updating based on free wave characteristics

Model updating is usually performed by minimizing a least-squares cost function quantifying the discrepancy between measured quantities and those obtained from the system model [3]. The objective of model updating is generally two-fold. First, model updating can be performed with the aim of estimating parameters on which little prior information is available. Second, by minimizing the discrepancy between the measurements and the model, it can also be assumed that the model after updating provides a better agreement with the actual dynamic behavior of the system.

The model updating approach of Simoen et al. [3, 1] is followed here. The measured quantities consist of the free wave characteristics. Assume that the model is characterized by a finite number n_θ of poorly known model parameters $\theta_{\mathrm{M},j}$. The model updating in this case consists of determining the optimal set of parameters $\boldsymbol{\theta}_\mathrm{M} = [\theta_{\mathrm{M},1}, \ldots, \theta_{\mathrm{M},n_\theta}]^\mathrm{T}$ that minimizes the following least-squares objective function:

$$\begin{aligned}\mathbf{F}(\boldsymbol{\theta}_\mathrm{M}, \omega_j) = &\sum_{k=1}^{n_\mathrm{w}} a_k \frac{(\bar{\lambda}_{\mathrm{p}k}(\omega_j) - \lambda_{\mathrm{p}k}(\boldsymbol{\theta}_\mathrm{M}, \omega_j))^2}{(\bar{\lambda}_{\mathrm{p}k}(\omega_j))^2} + \sum_{k=1}^{n_\mathrm{w}} b_k \frac{||\chi_{\mathrm{p}k}\bar{\boldsymbol{\psi}}_{\mathrm{p}k}(\omega_j) - \mathbf{L}\boldsymbol{\psi}_{\mathrm{p}k}(\boldsymbol{\theta}_\mathrm{M}, \omega_j)||_2^2}{||\chi_{\mathrm{p}k}\bar{\boldsymbol{\psi}}_{\mathrm{p}k}(\omega_j)||_2^2} \\ &+ \sum_{k=1}^{n_\mathrm{w}} c_k \frac{(\bar{\lambda}_{\mathrm{n}k}(\omega_j) - \lambda_{\mathrm{n}k}(\boldsymbol{\theta}_\mathrm{M}, \omega_j))^2}{(\bar{\lambda}_{\mathrm{n}k}(\omega_j))^2} + \sum_{k=1}^{n_\mathrm{w}} d_k \frac{||\chi_{\mathrm{n}k}\bar{\boldsymbol{\psi}}_{\mathrm{n}k}(\omega_j) - \mathbf{L}\boldsymbol{\psi}_{\mathrm{n}k}(\boldsymbol{\theta}_\mathrm{M}, \omega_j)||_2^2}{||\chi_{\mathrm{n}k}\bar{\boldsymbol{\psi}}_{\mathrm{n}k}(\omega_j)||_2^2}\end{aligned} \tag{11}$$

where n_w is the number of identified free wave pairs, ω_j is the considered frequency, $\bar{\lambda}_{\mathrm{p}k}(\omega_j)$, $\bar{\lambda}_{\mathrm{n}k}(\omega_j)$, $\bar{\boldsymbol{\psi}}_{\mathrm{p}k}(\omega_j)$, and $\bar{\boldsymbol{\psi}}_{\mathrm{p}k}(\omega_j)$ are the identified free wave characteristics (Section 2.2), with $\bar{\boldsymbol{\psi}}_{\mathrm{p}k}(\omega_j) = \mathbf{x}_{\mathrm{p}k}(\omega_j)/||\mathbf{x}_{\mathrm{p}k}(\omega_j)||_2$ and $\bar{\boldsymbol{\psi}}_{\mathrm{n}k}(\omega_j) = \mathbf{x}_{\mathrm{n}k}(\omega_j)/||\mathbf{x}_{\mathrm{n}k}(\omega_j)||_2$, and $\lambda_{\mathrm{p}k}(\boldsymbol{\theta}_\mathrm{M}, \omega_j)$, $\lambda_{\mathrm{n}k}(\boldsymbol{\theta}_\mathrm{M}, \omega_j)$, $\boldsymbol{\psi}_{\mathrm{p}k}(\boldsymbol{\theta}_\mathrm{M}, \omega_j)$, and $\boldsymbol{\psi}_{\mathrm{n}k}(\boldsymbol{\theta}_\mathrm{M}, \omega_j)$ are the corresponding computed quantities (Section 2.1). In addition, $\chi_{\mathrm{p}k}$ and $\chi_{\mathrm{n}k}$ are scaling factors which are introduced to obtain similar scaling of the measured and calculated free waves. These scaling factors are calculated as follows:

$$\chi_{\mathrm{p}k} = \frac{\bar{\boldsymbol{\psi}}_{\mathrm{p}k}^\mathrm{H}\mathbf{L}\boldsymbol{\psi}_{\mathrm{p}k}(\boldsymbol{\theta}_\mathrm{M})}{\|\bar{\boldsymbol{\psi}}_{\mathrm{p}k}\|_2^2}, \quad \chi_{\mathrm{n}k} = \frac{\bar{\boldsymbol{\psi}}_{\mathrm{n}k}^\mathrm{H}\mathbf{L}\boldsymbol{\psi}_{\mathrm{n}k}(\boldsymbol{\theta}_\mathrm{M})}{\|\bar{\boldsymbol{\psi}}_{\mathrm{n}k}\|_2^2} \tag{12}$$

where $^\mathrm{H}$ denotes the Hermitian transpose. Finally, a_k, b_k, c_k and d_k are user-defined weighting factors which are given a unit value throughout the remainder of this work.

In the construction of the objective function $\mathbf{F}(\boldsymbol{\theta}_\mathrm{M}, \omega_j)$ in Eq. (11), the calculated and observed free waves are matched by means of the following distance measure:

$$d_k(l) = \left| \frac{\mathrm{Im}(\bar{\mu}_k) - \mathrm{Im}(\mu_l(\boldsymbol{\theta}_\mathrm{M}) + 2\pi i \beta_{kl})}{\mathrm{Im}(\bar{\mu}_k)} \right| + (1 - \mathrm{MAC}(\bar{\boldsymbol{\psi}}_k, \mathbf{L}\boldsymbol{\psi}_l(\boldsymbol{\theta}_\mathrm{M}))) \tag{13}$$

where $\mathrm{Im}(\cdot)$ selects the imaginary part of the propagation constants, β_{kl} is an integer (-1, 0, or 1) which is determined as to minimize the first term in the right hand side of Eq. (13), and $\mathrm{MAC}(\cdot, \cdot)$ denotes the Modal Assurance Criterion [13], defined as:

$$\mathrm{MAC}(\bar{\boldsymbol{\psi}}_k, \mathbf{L}\boldsymbol{\psi}_l(\boldsymbol{\theta}_\mathrm{M})) = \frac{(\bar{\boldsymbol{\psi}}_k^\mathrm{H}\mathbf{L}\boldsymbol{\psi}_l(\boldsymbol{\theta}_\mathrm{M}))^2}{||\bar{\boldsymbol{\psi}}_k||_2^2 \; ||\mathbf{L}\boldsymbol{\psi}_l(\boldsymbol{\theta}_\mathrm{M})||_2^2} \tag{14}$$

The calculated mode l that results in the lowest value of $d_k(l)$ is matched to the observed free wave with given index k. Finally, note that the positive going waves ("p") and the negative going waves ("n") are matched individually.

When free wave characteristics at multiple frequencies ω_j are available, they can be considered simultaneously determining the optimal model parameters through the minimization of the total misfit:

$$\mathbf{G}(\boldsymbol{\theta}_{\mathrm{M}}) = \sum_{j=1}^{n_{\mathrm{f}}} \mathbf{F}(\boldsymbol{\theta}_{\mathrm{M}}, \omega_j) \tag{15}$$

with n_{f} the total number of frequencies considered in the model updating.

Similar to Section 2.2, the least-squares objective function in Eq. (15) is minimized by means of the Levenberg Marquardt optimization algorithm implemented in the non-linear least-squares optimization routine (lsqnonlin) contained in MATLAB [11].

3. The K032 viaduct

3.1. General information

The K032 viaduct consists of two curved integral bridges in parallel with each other, hereafter referred to as K032L and K032R (Fig. 5). Each bridge has 23 spans, most of them having a length of about 35 m. The total length of the viaduct is about 800 m. The two bridges are connected by a passway at the 19th and 20th span, allowing traffic to pass from one bridge to the other in case of emergency. For the sake of convenience, the global coordinate system xyz is aligned with the Lambert coordinate system, where the y-axis is pointing towards the geographical North. In addition, a right handed Local Coordinate System (LCS) $x'y'z'$ is assigned to every cross section of the deck, where the x'-axis and y'-axis are respectively aligned with the lateral and longitudinal direction of the bridge, see Fig. 5.

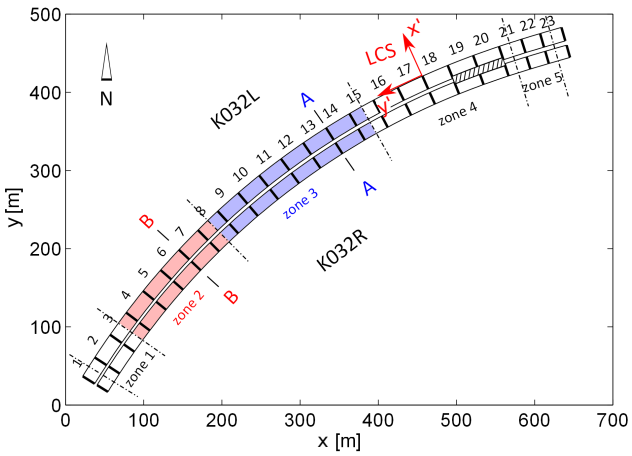

Fig. 5: Top view of the viaduct.

The two bridges are composed of concrete girders with solid cross section and concrete columns supported by pile foundations. As an example, Fig 6 shows cross sections A-A and B-B indicated in Fig. 5 for bridge K032R.

The viaduct is divided in five zones, also indicated in Fig. 5. Fig. 7 shows a schematic side view of bridge K032R, providing the geometry of the columns, the pile configurations, as well as concrete grade of the deck, the columns, and the piles for the different zones. The cross section

of the deck is the same throughout bridge K032R and has a width of 16.3 m, except for spans 19 and 20, where the passway is present. In the remainder of this work, the focus is on zones 2 and 3 of bridge K032R. Both zones are nearly periodic, with limited variations in the column and pile dimensions. They are therefore well-suited for the analysis based on free wave characteristics. The repetitive units of zones 2 and 3 of K032R are indicated in Fig. 7.

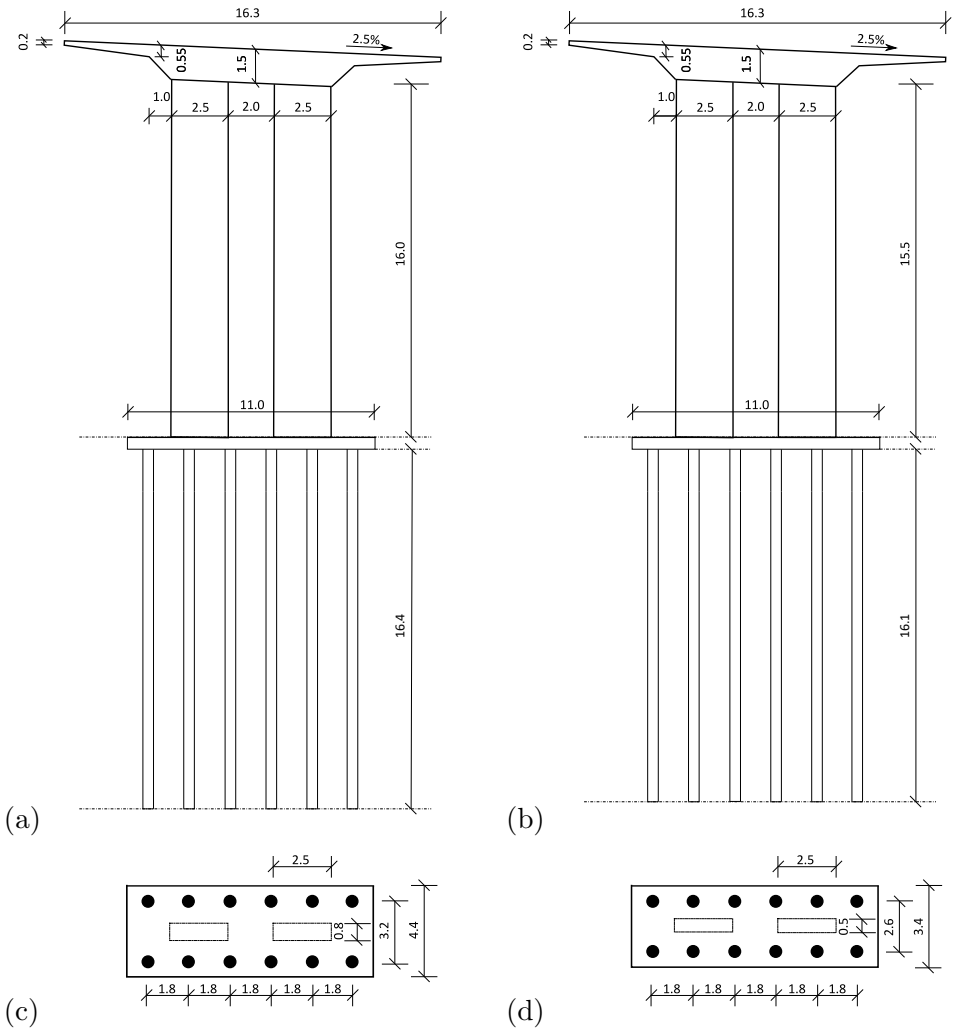

Fig. 6: (a) Cross section A-A for bridge K032R, (b) cross section B-B for bridge K032R, (c) top view of the pile foundation at cross section A-A and (d) top view of the pile foundation at cross section B-B. The dimensions are given in meter.

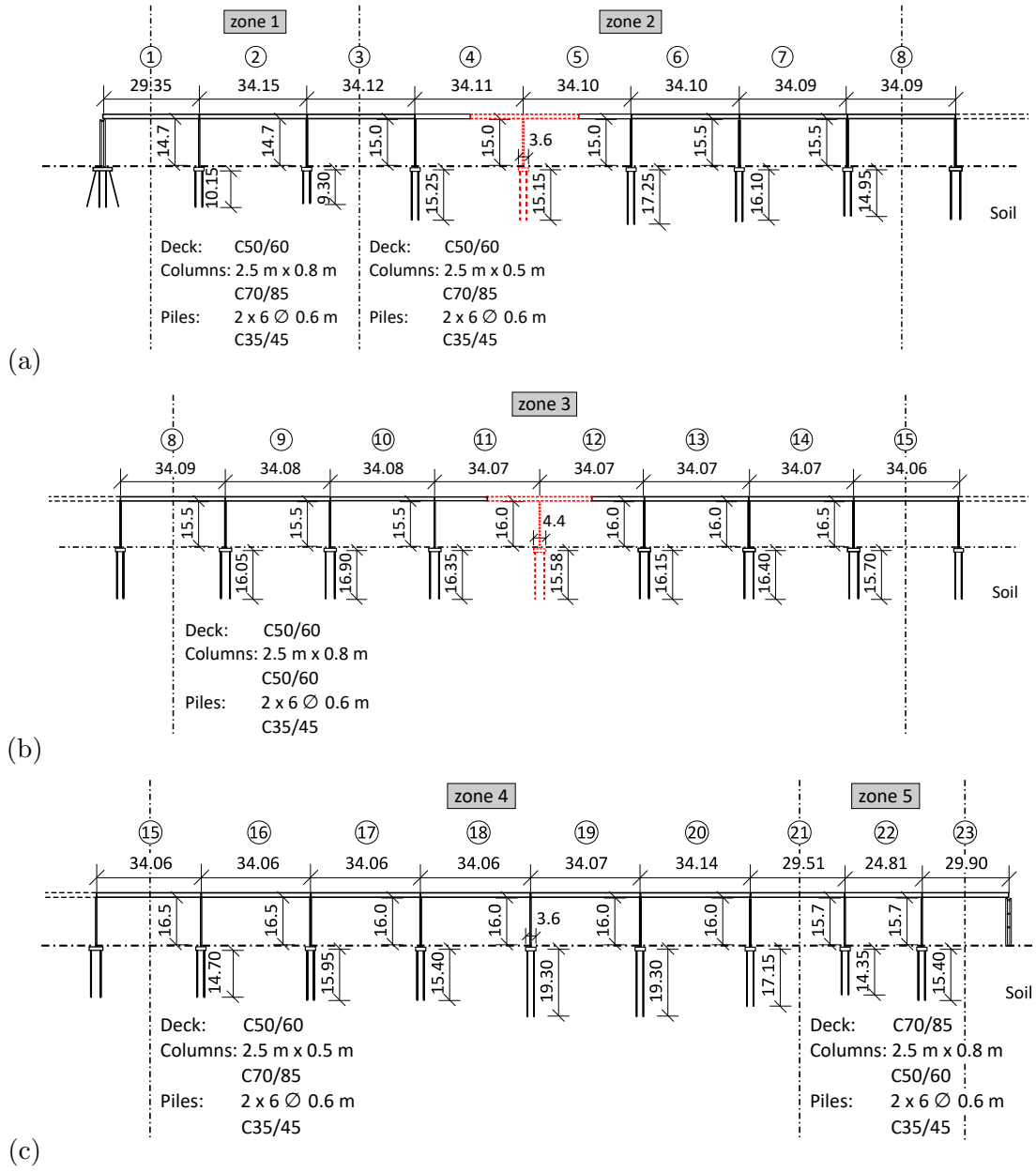

Fig. 7: Lateral view of bridge K032R with an indication of (a) zones 1 and 2, (b) zone 3, and (c) zones 4 and 5. The repetitive unit cells assumed for zones 2 and 3 are indicated using red dashed lines. The dimensions are given in meter.

3.2. Measurement setup

In situ measurements have been performed on 24 August 2017, prior to the opening of the A11 highway for traffic. The measurements are performed by means of nine wireless GeoSIG GMS-18 units and three wireless GeoSIG GMSplus units, which have been synchronized by means of GPS. Every GeoSIG unit includes a triaxial accelerometer, measuring the accelerations in three orthogonal directions. The three GMSplus units have three additional channels each, that can be used to record signals obtained from external sensors. Two GMSplus units are equipped with three external uniaxial accelerometers of type PCB 393B31 (10 V/g). The other GMSplus unit is equipped with an instrumented hammer of type PCB 086D50 with a mass of 5.5 kg. The remaining two external channels of this GMSplus unit are not used. The IEPE power supply for the uniaxial accelerometers and the hammer is provided by means of a PCB 480B21 ICP signal conditioner. The data acquisition is performed at a sampling rate of 200 Hz.

The GeoSIG units are placed on the asphalt layer of the bridge deck (Fig. 8a). The measurement directions of the internal triaxial accelerometer are aligned with the local coordinate system (LCS) of the corresponding bridge section (Fig. 5). The three accelerometers connected to both GMSplus units are installed on an aluminum block that is also placed on the asphalt layer (Fig. 8b). The uniaxial accelerometers measure in three orthogonal directions, which are aligned with the LCS. The hammer excitation is applied in the vertical (z) direction, in order to excite the vertical bending and torsional waves of the bridge.

(a) 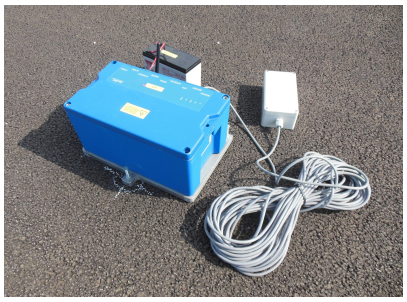 (b) 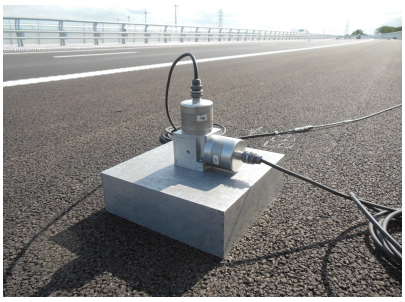

Fig. 8: (a) GeoSIG GMS-18 unit with external backup battery and GPS unit, and (b) aluminum block with two (out of three) uniaxial accelerometers PCB 393B31.

The measurements are performed in five setups, depicted in Fig. 9. The sensors are installed on two measurement lines along bridge K032R, denoted as lines A and B. The first two setups aim at the identification of the free wave characteristics at zone 2, with hammer excitation both at the left side (setup 1) and at the right side (setup 2). The GeoSIG sensors are installed at the interface between two unit cells. In the first two setups, the twelve recorders measure six units. The external uniaxial accelerometers have not been considered in the first two setups. Setups 3 and 4 are conducted in zone 3, with hammer excitation applied both at the left side (setup 3) and at the right side (setup 4). In setups 3 and 4, the external uniaxial accelerometers have been used to measure the response at the transition between zones 3 and 4, yielding a total of seven measured units for both setups. Finally, one additional setup was conducted (setup 5) to study the response at the transition between zones 2 and 3 due to excitation at the right side of zone 3.

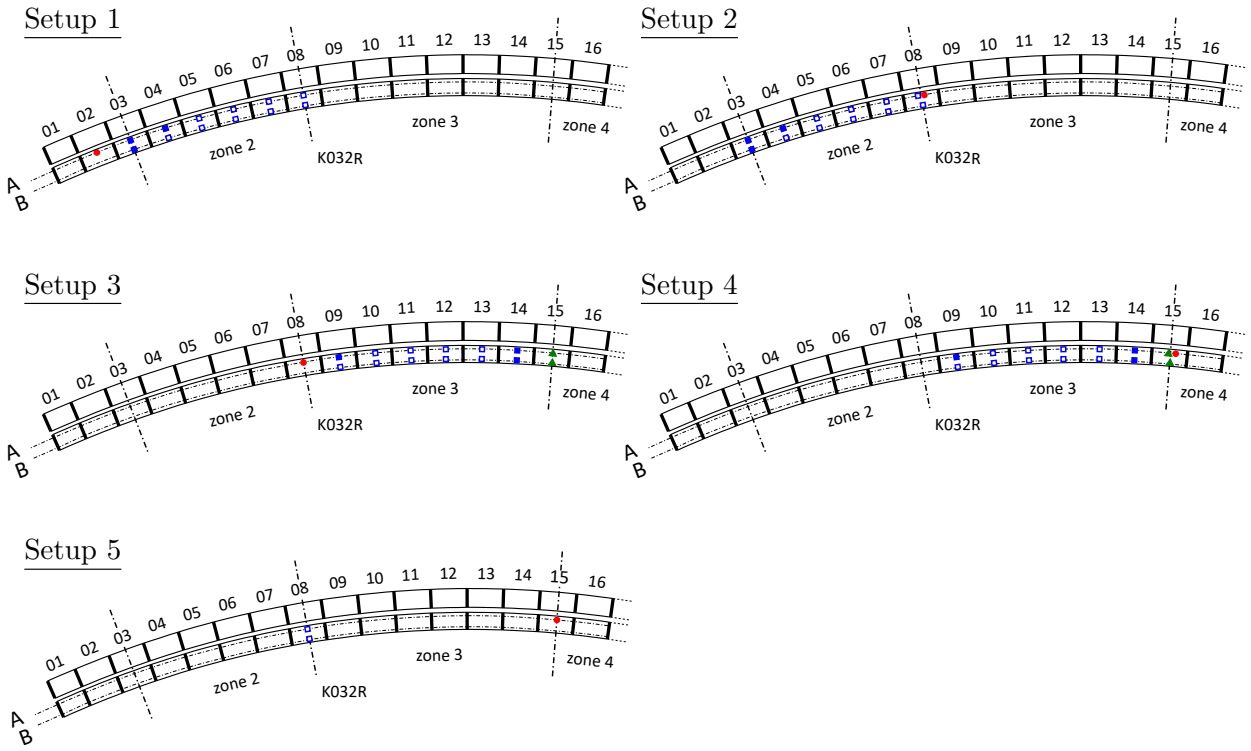

Fig. 9: Schematic overview of the measurement setups (blue hollow squares: GeoSIG GMS-18 units, blue solid squares: GeoSIG GMSplus units, green solid triangles: uniaxial accelerometers PCB 393B31, and red solid circles: hammer PCB 086D50).

The identification of the free wave characteristics requires accurate FRF estimates in the frequency range of interest. In general, any type of excitation can be used (e.g. hammer excitation, shaker excitation and dropping weight excitation), provided that the induced vibration levels exceed the ambient noise level. In the presented analysis of the K032 viaduct, heavy broadband hammer excitation was used, aiming for an application of the wave-based technique in a broad frequency range, including low frequencies (below 10 Hz) up to higher frequencies at 50 Hz. However, due to the large wind loads causing relatively high ambient vibration levels, the measured signal to noise ratio was found to be relatively low, as shown hereafter in Section 4. In order to reduce the influence of ambient noise and to enable the application of the wave-based technique, the H1 estimator is used in the calculation of the system FRFs. In addition, the frequency band is limited to frequencies above 15 Hz. This is further explained in Section 4.

4. Free wave identification

As previously mentioned, the signal to noise ratio of the measured accelerations under the considered impact loading is very low. This is especially the case for sensors at a large distance from the location where the loading is applied. The low signal to noise ratio is due to the fact that the bridge is fully exposed to wind loading, leading to continuous low frequency vibrations. As such, it was decided not to use the measured accelerations directly as input for the free wave identification, but alternatively to first compute the frequency response functions (FRFs) of the structure, which are then used to identify the free waves. As outlined next, the estimation of the FRFs involves averaging, which allows to significantly reduce the influence of the noise and vibration sources other than the impact loading.

The FRFs are calculated for the five setups individually using the so-called H1 estimator [14]. The following procedure is adopted:

- The full force and acceleration record for a given setup is first highpass filtered by means of a 5th order Butterworth filter with a highpass frequency of 0.5 Hz. The filter is applied both in the forward and reverse direction to remove all phase distortion. The aim of the filter is to remove low frequency components that are mainly dominated by measurement noise and attributed to wind loading.

- Software triggering is adopted to separate different impact events. The force signal is adopted as the triggering signal, using a threshold of 1 kN, a pre-trigger delay of 0.1 s, and a post-trigger delay of 0.9 s. As such, one triggered event has a length of 1 s or 200 samples. The number of impacts, hereafter referred to as n_e, slightly varies amongst the different setups. The lowest number of impacts is retrieved for setup 4 and equals 62.

- The FRF relating a given measured acceleration a_k to the vertical force p at the impact location, is estimated by averaging over the different events as follows:

$$H_k(\omega) = \sum_{l=1}^{n_\mathrm{e}} \frac{\hat{a}_{k,l}(\omega)\hat{p}_l^\mathrm{H}(\omega)}{\sum_{m=1}^{n_\mathrm{e}} \hat{p}_m(\omega)\hat{p}_m^\mathrm{H}(\omega)} \tag{16}$$

  where $\hat{p}_l(\omega)$ and $\hat{a}_{k,l}(\omega)$ denote the Fourier transform of respectively the input p and acceleration a_k for event l, which are computed by means of the fast Fourier transform (FFT) algorithm. The sample covariance of the H1 FRF estimate in Eq. (16) is computed according to [14]. The corresponding standard deviation for a given response a_k is denoted by σ_k.

As an example, Fig. 10 shows the amplitude of the estimated FRFs for setup 4, considering three sensors along measurement line A at different distances from the impact location. The $2\sigma_k$ sample uncertainty attributed to wind loading and sensor noise is plotted separately to provide an indication of the signal to noise ratio. As expected, the largest response amplitudes are obtained in the vertical (z') direction. For the three measurement locations, the FRF estimate according to the vertical direction exceeds the $2\sigma_k$ uncertainty threshold for all frequencies larger than 15 Hz. The signal to noise ratio, however, clearly decreases with the distance to the impact location. For sensors close to the impact location, there is also a noticeable lateral (x') response, which indicates that the eccentric vertical loading also mobilizes torsion of the bridge deck. For sensors at a distance above 100 m, however, the FRF estimate according to the lateral direction is dominated by noise. The longitudinal response y' is negligible and, therefore, also dominated by noise.

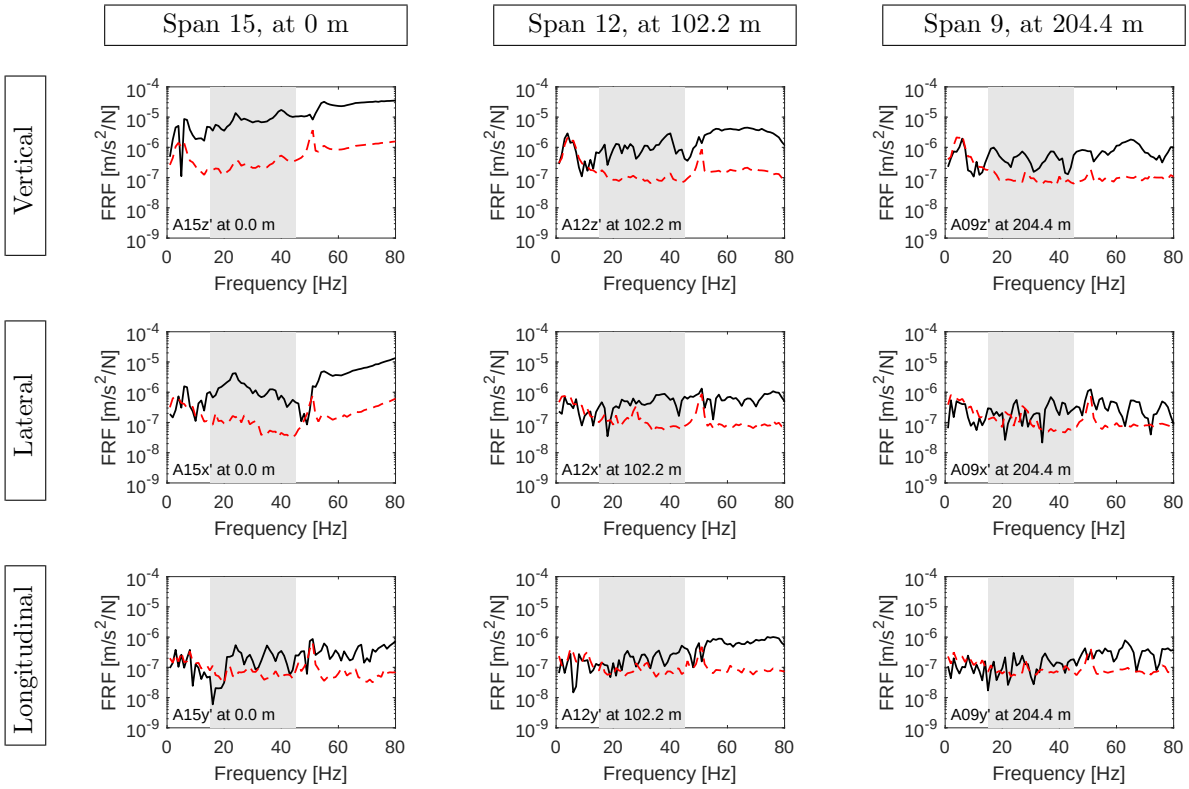

Fig. 10: Amplitude of the estimated FRFs for setup 4 at spans 15, 12, and 9 and measurement line A (solid black line). The $2\sigma_k$ sample uncertainty on the FRF amplitude is shown by a dashed red line. The measurement label and the distance to the impact location are given in the bottom left corner. Finally, the frequency range considered in the free wave identification and the model updating is indicated with a gray shading.

The FRFs obtained from the different setups are combined in four sets, shown in Fig. 11, each of them containing all measurements in a given zone (2 or 3) and a given side of the selected zone where the excitation is applied (left of right). The four sets of FRFs are considered separately in the free wave identification. In the following, the free wave identification is performed for the frequency range between 15 Hz and 45 Hz, in steps of 1 Hz. For this frequency range, the identified FRFs in Fig. 10 are clearly above the $2\sigma_k$ noise floor, especially for vertical and lateral acceleration measurements close to the impact location.

The free wave identification procedure outlined in Section 2.2 is now illustrated in detail for sets 3 and 4 (Fig. 11), which concern the free wave characteristics of zone 3. The free wave characteristics of zone 2 (sets 1 and 2) are also summarized and briefly discussed hereafter.

As previously explained in Section 2.2, the identification of the free wave pairs for a given number of repetitive units n_u involves solving the least squares optimization problem defined in Eq. (9). The maximum number of free wave pairs that can be identified is given by Eq. (10). In the present case, the number of response measurements for every unit n_m equals $2 \times 3 = 6$. For both sets 3 and 4, measurements are performed on 7 units, yielding $n_\mathrm{u} + 1 = 8$. In accordance to Eq. (10), the maximum number of free wave pairs that can be identified for zone 3, for every frequency and under the available set of measurements, equals 3.

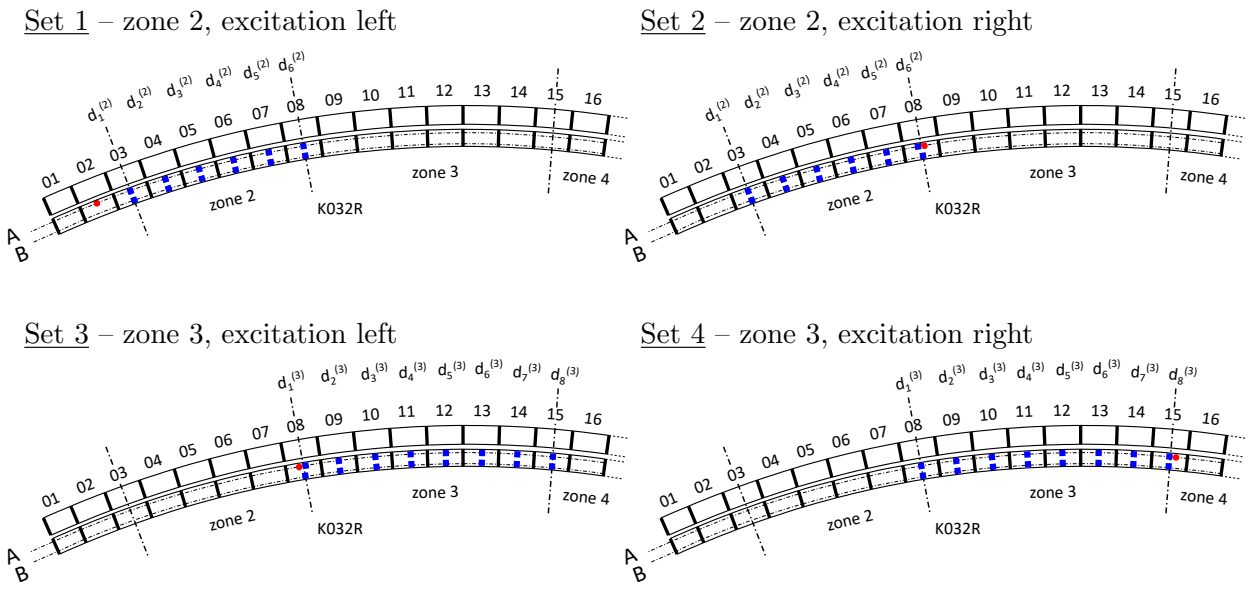

Fig. 11: Schematic overview of the different sets of FRFs considered in the free wave identification (blue solid squares: output locations, red solid circles: input locations).

Tables 1 and 2 show the identified propagation constants of the free wave pairs identified at 40 Hz, for set 3 (excitation at the left side of zone 3) and set 4 (excitation at the right side of zone 3), respectively. The number of free wave pairs n_w is increased from 1 to 3 in steps of 1, resulting in model orders $s = 2n_\mathrm{m} = 2,\ 4,$ and 6. The variation in the identified propagation constants and free wave vectors between two consecutive model orders s and $s+2$ is quantified by means of the following two stabilization indicators:

$$\delta^s_{\bar{\mu}_{\mathrm{p}k}} = \left| \frac{\bar{\mu}^s_{\mathrm{p}k} - \bar{\mu}^{s-2}_{\mathrm{p}k}}{\bar{\mu}^s_{\mathrm{p}k}} \right|, \qquad \delta^s_{\bar{x}_k} = \frac{\left|\left| \bar{\mathbf{x}}^s_k - \bar{\mathbf{x}}^{s-2}_k \right|\right|_2}{\left|\left| \bar{\mathbf{x}}^s_k \right|\right|_2}, \qquad \text{with} \quad \bar{\mathbf{x}}^s_k = \begin{bmatrix} \bar{\mathbf{x}}^s_{\mathrm{p}k} \\ \bar{\mathbf{x}}^s_{\mathrm{n}k} \end{bmatrix} \tag{17}$$

where $\bar{\mu}^s_{\mathrm{p}k}$, $\bar{\mathbf{x}}^s_{\mathrm{p}k}$ and $\bar{\mathbf{x}}^s_{\mathrm{n}k}$ are the identified free wave characteristics for a given model order s.

n_w [−]	s [−]	$\bar{\mu}_{\mathrm{p}1}$ [−]	$\delta^s_{\bar{\mu}_{\mathrm{p}1}}$ [%]	$\delta^s_{\bar{x}_1}$ [%]	$\bar{\mu}_{\mathrm{p}2}$ [−]	$\delta^s_{\bar{\mu}_{\mathrm{p}2}}$ [%]	$\delta^s_{\bar{x}_2}$ [%]	$\bar{\mu}_{\mathrm{p}3}$ [−]	$\delta^s_{\bar{\mu}_{\mathrm{p}3}}$ [%]	$\delta^s_{\bar{x}_3}$ [%]
1	2	−0.7034 − 2.6942i	–	–	–	–	–	–	–	–
2	4	−0.6009 − 2.8421i	6.20	28.9	−0.4881 − 0.0924i	–	–	–	–	–
3	6	−0.5475 − 2.8332i	1.87	9.84	−0.2092 − 0.1116i	117.91	93.12	−0.3026 − 0.7135i	–	–

Table 1: Results of the free wave identification at 40 Hz for set 3 (zone 3, excitation at the left side). Stable free wave pairs are indicated in blue. Selected free wave pairs are indicated using a rectangular text box.

As in a classical model analysis, the stabilization diagram is used. The variation of the propagation constants and the free wave vectors between consecutive model orders s enables distinguishing between stable free wave pairs and so-called spurious free wave pairs (see also [5]). A small variation of these free wave characteristics indicates stable and hence physical free wave pairs. A large variation indicates large uncertainty in the identification for the corresponding free wave pair, which can be attributed to insufficient excitation of this free wave pair or an underestimation of

n_w [−]	s [−]	$\bar{\mu}_{\mathrm{n}1}$ [−]	$\delta^s_{\bar{\mu}_{\mathrm{n}1}}$ [%]	$\delta^s_{\bar{x}_1}$ [%]	$\bar{\mu}_{\mathrm{n}2}$ [−]	$\delta^s_{\bar{\mu}_{\mathrm{n}2}}$ [%]	$\delta^s_{\bar{x}_2}$ [%]	$\bar{\mu}_{\mathrm{n}3}$ [−]	$\delta^s_{\bar{\mu}_{\mathrm{n}3}}$ [%]	$\delta^s_{\bar{x}_3}$ [%]
1	2	$0.5705 + 2.8224\mathrm{i}$	–	–	–	–	–	–	–	–
2	4	$0.5511 + 2.8288\mathrm{i}$	0.71	9.52	$0.2738 + 0.0725\mathrm{i}$	–	–	–	–	–
3	6	$0.5591 + 2.8299\mathrm{i}$	0.28	4.05	$0.4938 - 0.1330\mathrm{i}$	58.87	34.97	$0.1555 + 1.0244\mathrm{i}$	–	–

Table 2: Results of the free wave identification at 40 Hz for set 4 (zone 3, excitation at the right side). Stable free wave pairs are indicated in blue. Selected free wave pairs are indicated using a rectangular text box.

the true system order. A threshold of 10% for $\delta^s_{\bar{\mu}_{\mathrm{p}k}}$ and 25% for $\delta^s_{\bar{x}_k}$ as proposed in [5] is adopted here. Those threshold values result in a single pair of free stable waves for both sets 3 and 4. The physical nature and the stability of those free waves is confirmed by the fact that the same type of free waves is identified for all considered frequencies in the range from 38 to 44 Hz, as also shown hereafter. Finally, note that identified free wave pairs which do not meet the imposed stabilization criteria for $s = 3$ may turn out to be stable when further increasing the model order s. This, however, would require further increasing the number of measured unit cells n_u.

Figs. 12 and 13 show the identified free wave vectors at 40 Hz for set 3 and set 4, respectively, considering a model order $s = 6$. Both stable and spurious modes are included. The free wave vectors are rescaled to reflect their contribution to the measured response. For both sets, the stable free wave pairs (left) correspond to a torsional wave that has the largest contribution to the response. It is also observed that the spurious free wave pairs for both sets (middle and right) are characterized by a very large wavelength, which is only partially covered by the sensors. Finally, it is observed that the positive going waves dominate the response for set 3 (excitation at the left side of zone 3) and similarly that the negative going waves dominate the response for set 4 (excitation at the right side of zone 3). The contributions of the reflected counterparts, i.e. the negative going waves for set 3 and positive going waves for set 4, are negligible.

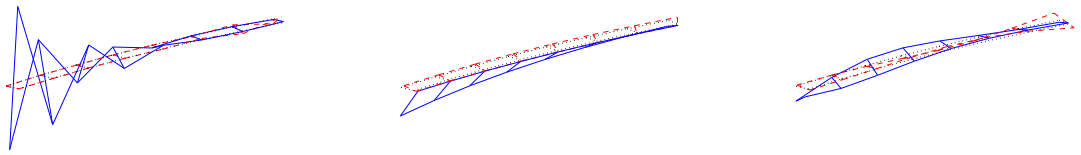

$-0.5475 - 2.8332\mathrm{i}$ $\quad -0.2092 - 0.1116\mathrm{i}$ $\quad -0.3026 - 0.7135\mathrm{i}$

Fig. 12: Imaginary part of the positive going (solid blue lines) and negative going (dashed red lines) free waves identified at 40 Hz for set 3 (zone 3, excitation at the left side). The wave propagation constant $\bar{\mu}_{\mathrm{p}k}$ corresponding to the positive going wave is indicated below the figures. Stable free wave pairs are indicated in blue font color.

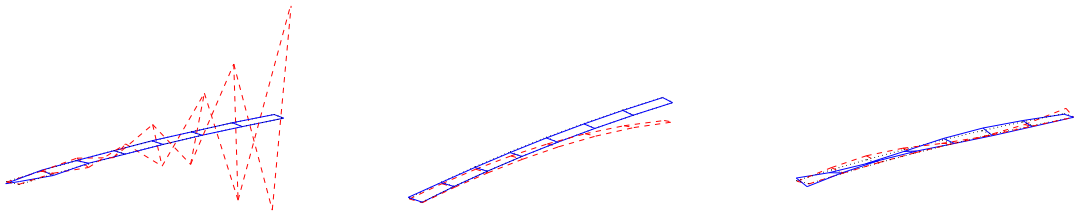

$0.5591 + 2.8299\mathrm{i}$ $0.4938 - 0.1330\mathrm{i}$ $0.1555 + 1.0244\mathrm{i}$

Fig. 13: Imaginary part of the positive going (solid blue lines) and negative going (dashed red lines) free waves identified at 40 Hz for set 4 (zone 3, excitation at the right side). The wave propagation constant $\bar{\mu}_{\mathrm{n}k}$ corresponding to the negative going wave is indicated below the figures. Stable free wave pairs are indicated in blue font color.

The stable torsional free waves in zone 3 identified for sets 3 and 4 are slightly different from each other, both in terms of propagation constant and free wave vector. This might result from the fact that zone 3 is not perfectly periodic due to small differences in the column lengths, pile lengths and soil properties, from the contribution of other free waves that could not be identified due to the limited model order, or from noise in the measurements.

The previously presented and illustrated methodology is now repeated for all frequencies between 15 Hz and 45 Hz and considering steps of 1 Hz. For frequencies below 38 Hz, it was not possible to identify stable free wave pairs occurring both in sets 3 and 4. For all frequencies between 38 Hz and 44 Hz, one stable pair of free waves could be identified, each of them corresponding to torsion of the bridge deck. The identified propagation constants are listed in Table 3. The corresponding free waves are shown in Fig. 14. As previously observed, small differences between the torsional waves obtained for sets 3 and 4 are present, which may be attributed to a lack of periodicity in zone 3 and estimation inaccuracies.

Frequency [Hz]	$\bar{\mu}_{\mathrm{p}1}$ (set 3) [−]	$\bar{\mu}_{\mathrm{n}1}$ (set 4) [−]
38	$-1.0173 - 2.1873\mathrm{i}$	$0.7330 + 2.0586\mathrm{i}$
39	$-0.7105 - 2.4050\mathrm{i}$	$0.6250 + 2.4098\mathrm{i}$
40	$-0.5475 - 2.8332\mathrm{i}$	$0.5591 + 2.8299\mathrm{i}$
41	$-0.6704 + 2.9798\mathrm{i}$	$0.6324 - 3.0734\mathrm{i}$
42	$-0.8618 + 2.7180\mathrm{i}$	$0.7350 - 2.8837\mathrm{i}$
43	$-0.9538 + 2.5433\mathrm{i}$	$0.6673 - 2.6902\mathrm{i}$
44	$-0.8863 + 2.4005\mathrm{i}$	$0.5653 - 2.3840\mathrm{i}$

Table 3: Propagation constants of the free wave pairs identified for zone 3 between 38 Hz and 44 Hz when the excitation is applied at the left (set 3) and right (set 4).

The same procedure is adopted for the free wave identification in zone 2. In this zone, six units are measured ($n_{\mathrm{u}} + 1 = 7$), resulting in a maximum of two pairs of free waves that can be identified at each frequency. Similar to zone 3, the identification is performed for all frequencies between 15 Hz and 45 Hz in steps of 1 Hz. It is found that the identification results are generally less accurate when compared to those obtained for zone 3, resulting in a larger variation between the free wave pairs obtained for different model orders. This is probably due to the fact that less units are measured for zone 2. The threshold on the free wave vector stabilization indicator $\delta^s_{\bar{x}_k}$ is increased from 25% to 60% to enable picking up one pair of stable free waves. Even after this

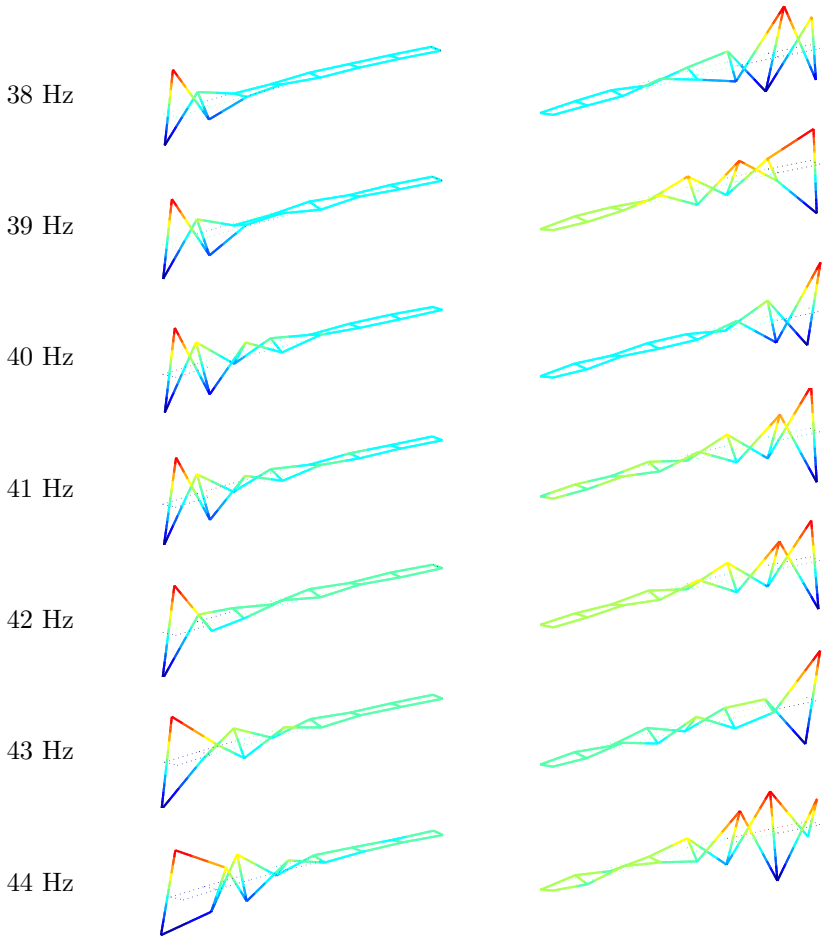

Fig. 14: Imaginary part of the identified positive going (left) and negative going (right) torsional free waves in zone 3 at frequencies 38 Hz to 44 Hz. The positive going waves are obtained from set 3. The negative going waves are obtained from set 4.

relaxation, however, stable free wave pairs are only identified for 40 Hz, 41 Hz and 42 Hz. For the other frequencies, no stable free wave pairs are retrieved. The identified propagation constants of zone 2 are listed in Table 4. The corresponding free wave vectors are shown in Fig. 15. As was the case for zone 3, the identified free waves in this case correspond to torsion of the bridge deck. The fact that very similar free waves are obtained for the three different frequencies (40 Hz, 41 Hz and 42 Hz) confirms the physical nature of the identified free waves, despite the relaxation of the stabilization indicator $\delta^s_{\bar{x}_k}$.

5. Model updating

This section presents the model updating for the K032 viaduct. First, Section 5.1 describes the preliminary unit cell finite element model and its corresponding calculated free waves (in accordance to Section 2.1). Next, Section 5.2 presents the sensitivity analysis that is adopted to select relevant parameters to be determined in the model updating. Section 5.3 presents the results of the model updating. Finally, Section 5.4 discusses complementarity of the presented approach with classical model updating based on modal characteristics.

Frequency [Hz]	$\bar{\mu}_{\mathrm{p1}}$ (set 1) [−]	$\bar{\mu}_{\mathrm{n1}}$ (set 2) [−]
40	$-0.5703 + 2.9007\mathrm{i}$	$0.7025 + 3.0446\mathrm{i}$
41	$-0.6914 + 2.6279\mathrm{i}$	$0.7456 - 2.8758\mathrm{i}$
42	$-0.8871 + 2.3935\mathrm{i}$	$0.8853 - 2.6380\mathrm{i}$

Table 4: Propagation constants of the free wave pairs identified for zone 2 between 40 Hz and 42 Hz when the excitation is applied at the left (set 1) and right (set 2).

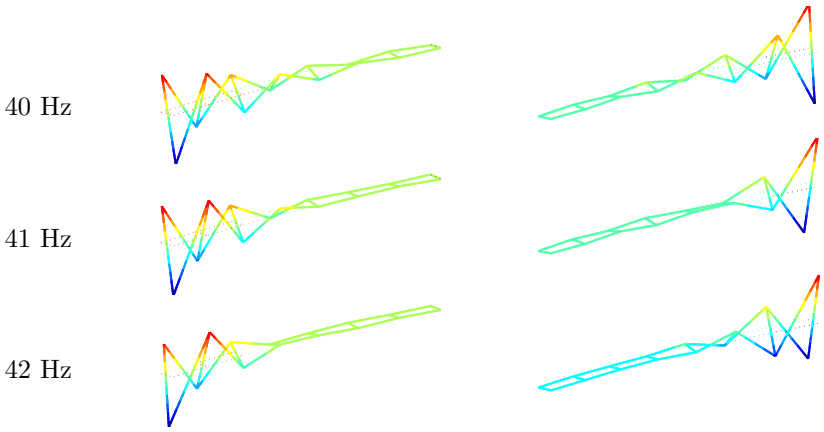

Fig. 15: Imaginary part of the identified positive going (left) and negative going (right) torsional free waves in zone 2 at frequencies 40 Hz to 42 Hz. The positive going waves are obtained from set 1. The negative going waves are obtained from set 2.

5.1. Preliminary finite element model

This section describes the finite element model (FEM) representing a unit cell of zone 3. The model used in the model updating for zone 2 is constructed similarly but is not discussed here.

The preliminary FEM of the unit cell of zone 3 of bridge K032R is based on the blueprints of the structure. The model is constructed in two stages. In the first stage, the bridge deck and the columns are modeled in ANSYS [15]. The model, shown in Fig. 16, is composed of the ANSYS solid element SOLID45. The stiffness matrix $\mathbf{K}$ and mass matrix $\mathbf{M}$ are extracted from the (detailed) ANSYS model and coupled in a second step in MATLAB to a separate model of the pile foundation, which is developed using the MATLAB toolbox StaBIL [16, 17]. The piles are modeled using beam elements. The surrounding soil is modeled by static distributed springs with lateral stiffness ($k^{\mathrm{s}}_{\mathrm{lateral}}$), axial stiffness ($k^{\mathrm{s}}_{\mathrm{axial}}$) and end-bearing axial stiffness ($k^{\mathrm{s}}_{\mathrm{end}}$). These stiffnesses are estimated according to API practice 2A-WSD [18] using the soil properties provided by Databank Ondergrond Vlaanderen [19]. The pile cap is assumed to be rigid and the column base is fixed at the center of the pile cap. The static impedance matrix is calculated from the StaBIL model of the pile foundation, which is then coupled to the ANSYS model of the bridge deck and columns.

As an example, Fig. 17 shows the calculated free waves obtained from the model of zone 3 at 40 Hz, for a column length of 16 m. Frequency-independent hysteretic damping is assumed.

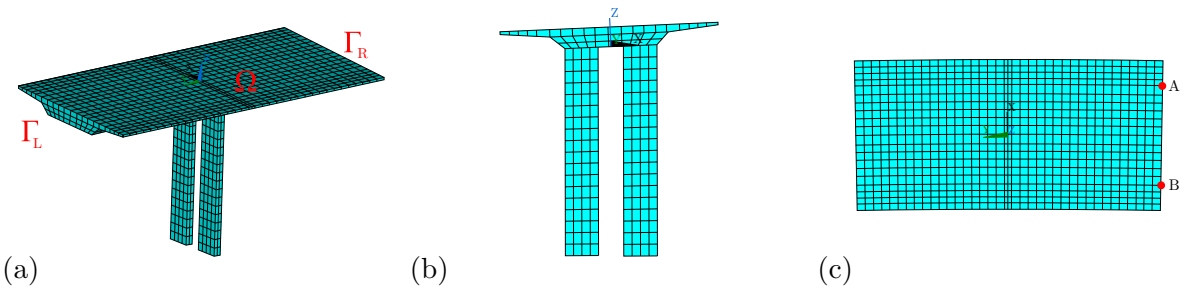

Fig. 16: (a) 3D view, (b) longitudinal view and (c) top view of the ANSYS model of one unit cell at zone 3.

The corresponding equation of motion is given by $(\mathbf{K} + i\eta\mathbf{K} - \omega^2\mathbf{M})\hat{\mathbf{u}} = \hat{\mathbf{F}}$, with η the hysteretic

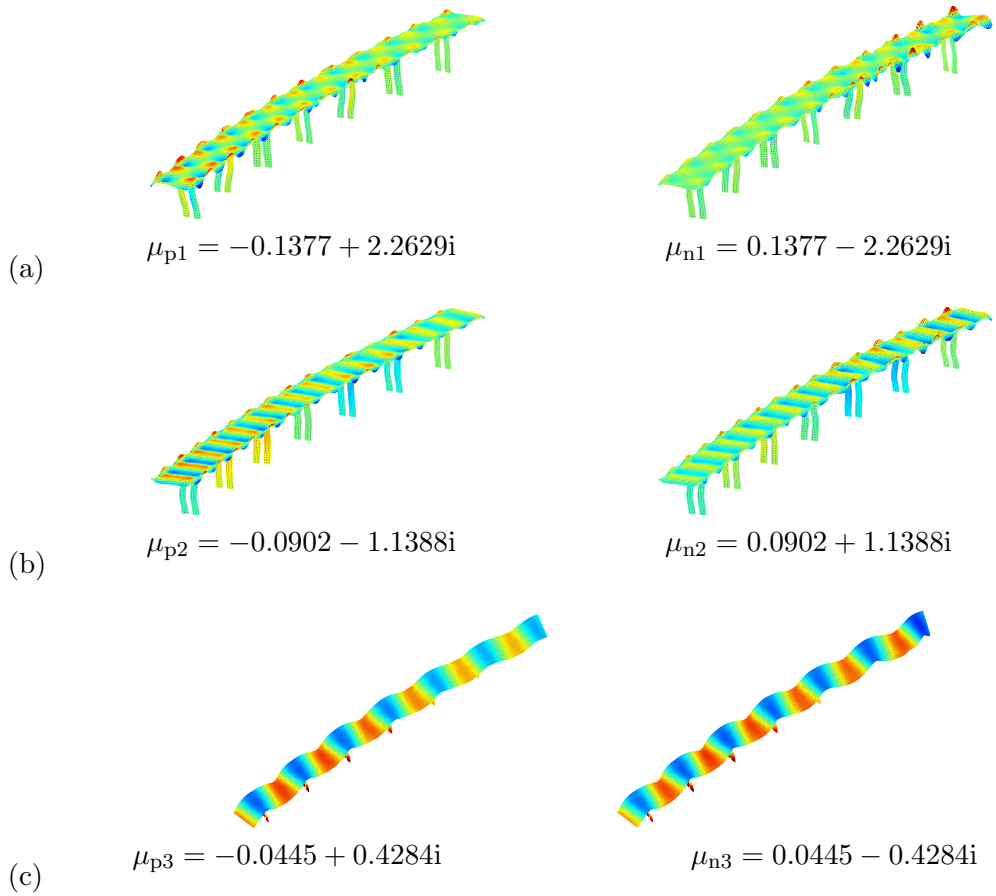

Fig. 17: Imaginary part of the calculated positive going (left) and the corresponding negative going (right) free waves at 40 Hz, obtained from the preliminary FEM of zone 3 and assuming column length 16 m.

damping factor, which is initially assigned the value 0.02. The effective Young's moduli of the deck, column and piles are taken as $E_{\text{deck}} = E_{\text{column}} = 37$ GPa and $E_{\text{pile}} = 34$ GPa. Only free wave pairs with a pronounced motion of the bridge deck are retained from the model. The first pair of free waves ($\mu_{n1} = 0.1377 - 2.2629i$, Fig. 17a) involves local bending of the deck, with nearly anti-symmetric bending motion around the longitudinal axis. The second pair ($\mu_{n2} = 0.0902 + 1.1388i$,

Fig. 17b) shows a local bending wave symmetric around the longitudinal axis. Finally, the third pair ($\mu_{n3} = 0.0445 - 0.4284i$, Fig. 17c) involves lateral bending of the deck in combination with local vertical bending.

By means of the distance measure $d_k(l)$ in Eq. (13), the identified free waves can be linked to those obtained from the FEM. For example, at 40 Hz, the identified negative going free wave shown in Fig. 14 is matched with the calculated local bending free wave obtained from the preliminary model shown in Fig. 17a. A high MAC value of 0.94 is obtained, indicating a good match. The identified and calculated propagation constants, however, are significantly different; $\bar{\mu}_{nk} = 0.5591 + 2.8299i$, $\mu_{nl} + 2\pi i\beta_{kl} = 0.1377 - 2.2629i + 2\pi i = 0.1377 + 4.0203i$ ($\beta_{kl} = 1$). As will be shown in subsection 5.3, the model updating will reduce this difference, leading to an improved match between the model and the actual system behavior.

5.2. Sensitivity analysis

The parameters assumed variable in the model updating are determined by means of a sensitivity analysis. Six different parameters are considered, which are 1) the hysteretic damping factor ($\theta_1\eta$), 2) the effective stiffness of the concrete deck ($\theta_2 E_{\text{deck}}$), 3) the effective stiffness of the columns ($\theta_3 E_{\text{column}}$), 4) the effective stiffness of the piles ($\theta_4 E_{\text{pile}}$), 5) the lateral stiffness provided by the soil ($\theta_5 k^{\text{s}}_{\text{lateral}}$) and 6) the axial and end bearing stiffness of the soil ($\theta_6 k^{\text{s}}_{\text{axial,end}}$). The sensitivities are calculated for $\theta_j = 1$, $j = 1, \ldots, 6$, which corresponds to the preliminary model introduced in Section 5.1.

The sensitivities of the free waves in the frequency range between 38 Hz and 44 Hz are expected to be similar, since the free waves are all of the same type. The sensitivity analysis is therefore only performed at 40 Hz. The sensitivities of the eigenvalues of the negative going free waves ($\lambda_{N1} = e^{\mu_{N1}}$) are listed in Table 5. The eigenvalues are found to be very sensitive to the stiffness of the concrete deck (θ_2). They are less sensitive to the stiffness of the columns (θ_3) and the damping (θ_1) and nearly insensitive to the stiffness of the foundation (θ_4, θ_5, θ_6). In order to better understand the influence of the parameters on the wave attenuation, the sensitivities of the corresponding propagation constants are calculated as well. It is found that the stiffness of the deck has a large influence on the imaginary part of the propagation constant, as it characterizes the bending and torsional wavelength. The real part of the propagation constant is very sensitive to damping, as it influences the attenuation of the free wave.

Parameter	$\frac{\partial \lambda_{n1}}{\partial \theta}$	$\frac{\partial \mu_{n1}}{\partial \theta}$
θ_1	$-0.104 - 0.118i$	$0.137 - 0.004i$
θ_2	$-5.155 + 4.292i$	$-0.013 - 5.845i$
θ_3	$-0.859 + 0.796i$	$-0.056 - 1.019i$
θ_4	$-0.080 + 0.071i$	$-0.003 - 0.093i$
θ_5	$-0.022 + 0.016i$	$0.001 - 0.023i$
θ_6	$-0.101 + 0.107i$	$-0.015 - 0.127i$

Table 5: The sensitivity of the eigenvalue λ_{n1} and the corresponding propagation constant μ_{n1} of the negative going free waves at 40 Hz.

The sensitivity of the corresponding free wave shapes is also calculated and plotted in Fig. 18. The free wave shapes are most sensitive to the stiffness of the concrete deck (θ_2). To a minor

extent, they are also affected by the stiffness of the columns (θ_2). They are found to be nearly insensitive to the foundation stiffness (θ_4, θ_5, θ_6) and the damping (θ_1).

Since it is found that the considered free wave characteristics are all insensitive to the foundation stiffness, the set of parameters considered in the model updating is limited to the damping (θ_1), the stiffness of the concrete deck (θ_2), and the stiffness of the columns (θ_3). The other parameters are assigned constant values ($\theta_4 = \theta_5 = \theta_6 = 1$).

A first attempt was made to update the three parameters θ_1, θ_2, and θ_3, parameterizing respectively the damping, the stiffness of the bridge deck, and the bridge deck of the columns. This updating yielded unrealistic values for the Young's moduli of the bridge deck and the columns. The stiffness of the bridge deck is underestimated, while the stiffness of the columns is highly overestimated. This is most probably due to over-parameterization, which leads to ill-conditioning of the problem. Since the sensitivity of the free wave parameters to the deck stiffness (θ_2) is much larger than the sensitivity to the column stiffness (θ_3) it was decided to additionally fix the the column stiffness, i.e. $\theta_3 = 1$, leaving only two parameters θ_1 and θ_2 to be determined in the model updating.

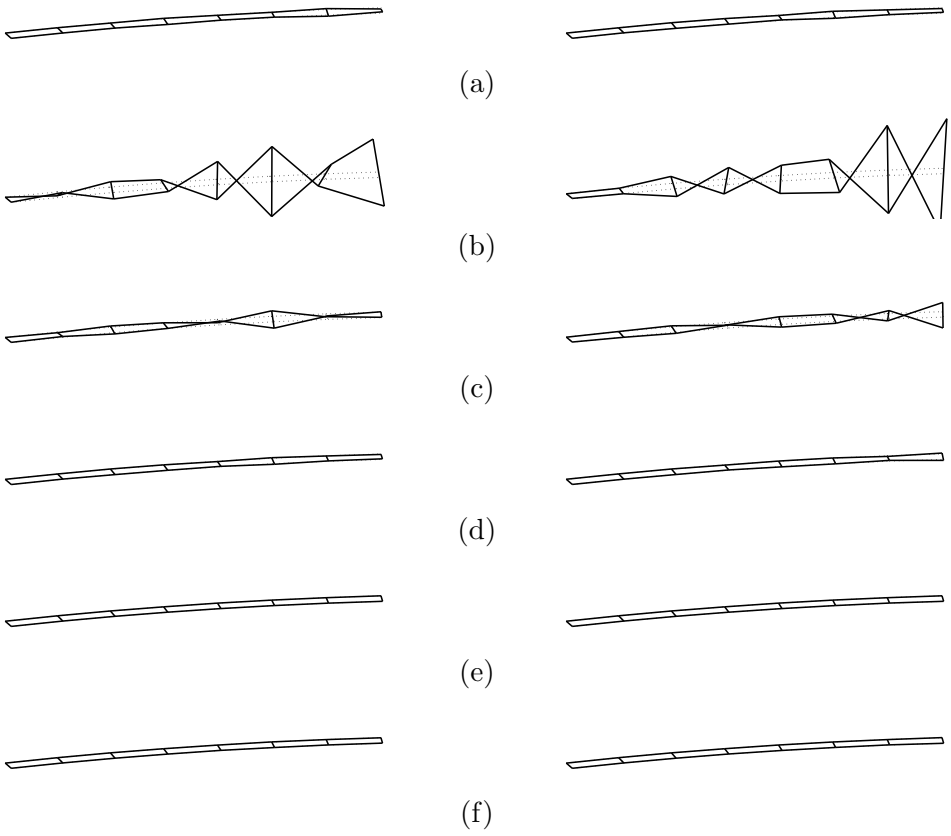

Fig. 18: The real part (left) and imaginary part (right) of the sensitivity of the negative going free wave at 40 Hz with respect to (a) θ_1, (b) θ_2, (c) θ_3, (d) θ_4, (e) θ_5, and (f) θ_6.

5.3. Results model updating

As previously mentioned in Section 2.3, the model updating is performed by means of an iterative gradient-based optimization procedure. In order to reduce the computational time, the stiffness matrix $\mathbf{K}$ of the ANSYS model is partitioned into two parts, $\mathbf{K}_{\text{deck}}$ and $\mathbf{K}_{\text{column}}$, with $\mathbf{K} = \theta_{\text{M},2}\mathbf{K}_{\text{deck}} + \mathbf{K}_{\text{column}}$. The matrices $\mathbf{K}_{\text{deck}}$, $\mathbf{K}_{\text{column}}$, and $\mathbf{M}$ are extracted from ANSYS prior to the model updating. As such, the calculation of the matrices $\mathbf{K}$ and $\mathbf{M}$ of the bridge deck and the columns in the iterations of the model updating can be entirely performed in MATLAB and does not require calling ANSYS in each step of the iterative model updating process.

As the column length in zone 3 varies from 15.5 m for the leftmost columns up to 16.5 m for the rightmost columns (Fig. 7), it was decided to consider two different unit cell models in the model updating. A unit cell model with column length 15.5 m is adopted when considering free wave characteristics of the positive going waves for zone 3, which are mainly present in the left part of zone 3 (see also Fig. 14, left sub-figures). A unit cell model with column length 16 m is adopted when considering free wave characteristics of the negative going waves for zone 3, which are mainly present in the right part of zone 3 (see also Fig. 14, right sub-figures). In the updating for zone 2, a column length of 15 m and 15.5 m is assumed for the positive and negative going free waves, respectively.

Four different sets are initially considered in the model updating, corresponding to the positive and negative going waves for both zones 2 and 3. The aim of considering these sets separately rather than including them in one objective function is to enable cross validation of the results.

Table 6 presents the results of the model updating for zones 3 and 2. In the updating for zone 3, the identified free wave characteristics from 38 Hz to 44 Hz are accounted for. In the updating for zone 2, the identified free wave characteristics from 40 Hz to 42 Hz are accounted for. Although slightly different parameter values are obtained for the four cases reported in Table 6, the results are clearly in line with each other. The updating increases the damping with about 400%, while the effective stiffness of the bridge deck is increased by about 20%. The latter may be attributed to the steel reinforcement and the pre-stressing of the bridge deck, which have not been explicitly accounted for in the initial FEM. It is expected that the results obtained for zone 2 are less accurate than those obtained for zone 3. This is at least partly due to the less accurate identification of the free waves in zone 2, which can be attributed to the lower number of measured units (Section 4). In addition, less free waves are taken into account in the updating of zone 2, as only three pairs of free waves at 40 Hz, 41 Hz, and 42 Hz are obtained from the identification.

		Zone 3	Zone 3	Zone 2	Zone 2	Combined sets
Column length [m]		15.5	16.0	15.0	15.5	–
$\theta_{\text{M},1}$ [-]	initial value	1	1	1	1	1
	updated value	6.64	4.64	5.91	6.15	5.40
η [-]	initial value	0.02	0.02	0.02	0.02	0.02
	updated value	0.13	0.09	0.12	0.12	0.11
$\theta_{\text{M},2}$ [-]	initial value	1	1	1	1	1
	updated value	1.20	1.24	1.09	1.15	1.19
E_{deck} [Gpa]	initial value	37	37	37	37	37
	updated value	44.29	45.91	40.33	42.55	44.03

Table 6: Overview of the initial and updated parameter values obtained from the model updating for zones 3 and 2.

In order to enable the interpretation of the damping values η listed in Table 6, the relation between the damping parameter η in the assumed case of hysteretic damping and the modal damping ratios ξ_j in the commonly adopted case of proportional damping is established. The equation of motion in the case of hysteretic damping is given by:

$$(\mathbf{K} + i\eta\mathbf{K} - \omega^2\mathbf{M})\hat{\mathbf{u}}(\omega) = \hat{\mathbf{F}}(\omega) \tag{18}$$

Performing modal decomposition, premultiplying the modal equation for a given mode k with φ_k^{T}, and accounting for the orthogonality of the eigenmodes φ_k with respect to the stiffness and mass matrices yields:

$$(\omega_k^2 + i\eta\omega_k^2 - \omega^2)\hat{\boldsymbol{\alpha}}_k(\omega) = \varphi_k^{\mathrm{T}}\hat{\mathbf{F}}(\omega) \tag{19}$$

where ω_k is the kth eigenfrequency, ω is the considered angular frequency, and $\hat{\boldsymbol{\alpha}}_k$ is the kth modal coordinate.

Alternatively, in the case of proportional damping, the modal equation is given by:

$$(\omega_k^2 + 2i\xi_k\omega_k\omega - \omega^2)\hat{\boldsymbol{\alpha}}_k(\omega) = \varphi_k^{\mathrm{T}}\hat{\mathbf{F}}(\omega) \tag{20}$$

with ξ_k the modal damping ratio of mode k. The damping in both models is identical when the following equality holds:

$$\eta = \frac{2\xi_k\omega}{\omega_k} \tag{21}$$

At the natural frequency ($\omega = \omega_k$), both modal contributions are identical if $\xi_k = \eta/2$. As such, the identified hysteretic damping factor $\eta = 0.12$ corresponds to a modal damping ratio $\xi_k = 0.06$ (i.e. 6% modal damping), which is high but still in a reasonable range for concrete structures. In addition, the frequencies considered in the identification are located around 40 Hz, which is relatively high compared to the frequencies that are usually considered in system identification of civil engineering structures. This could also explain the relatively high damping value, since damping typically increases with frequency.

Fig. 19 shows the evolution of the residual of the objective function in Eq. (15) for the updating of the parameters in zone 3. In both cases, a clear reduction of the residual value is observed, showing how the match between the measured and calculated free waves is improved. This is confirmed by Table 7 and Fig. 20, which compare the propagation constants and free wave vectors of the identified negative going free waves in zone 3 to those obtained from the initial and updated FEM. In the latter model, the parameters values are taken as the average of the values obtained for the two different column lengths (Table 6). It is found that this averaging step does not significantly affect the "match" between the measurements and the updated FEM. It is apparent that the updated model is in much better agreement with the measurements than the initial FEM.

As a further validation of the presented approach, the four sets are now combined in a single objective function. The results of the corresponding model updating is also shown in Table 6. As expected, the resulting updated parameters for the combined sets ($\theta_1 = 5.40$ and $\theta_2 = 1.19$) lie in between the updated parameter values obtained for the cases where each of the four sets is considered separately.

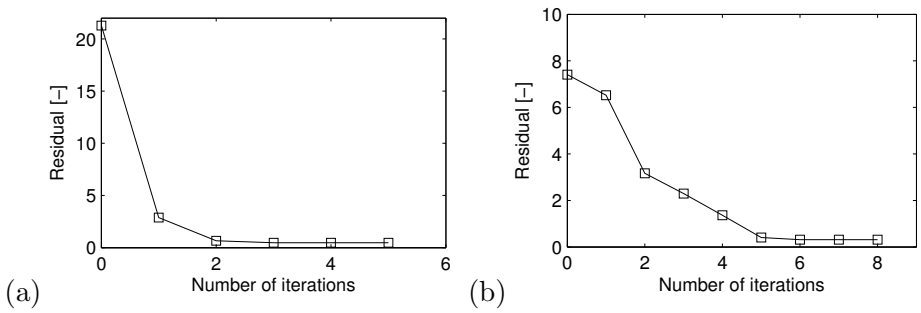

Fig. 19: Residual of the objective function in Eq. (15) for the updating of the preliminary unit cell model of zone 3 with a column length of (a) 15.5 m and (b) 16 m.

Frequency	$\bar{\mu}_{n1}$ [-]	μ_{n1} [-]	μ^*_{n1} [-]
38 Hz	$0.7330 + 2.0586i$	$0.1768 + 3.3010i$ (62.3%)	$0.7222 + 2.1786i$ (5.5%)
39 Hz	$0.6250 + 2.4098i$	$0.1378 + 3.6634i$ (54.0%)	$0.7235 + 2.5162i$ (5.8%)
40 Hz	$0.5591 + 2.8299i$	$0.1377 + 4.0203i$ (43.8%)	$0.7316 + 2.8446i$ (6.0%)
41 Hz	$0.6324 - 3.0734i$	$0.1488 - 1.9011i$ (40.4%)	$0.7479 - 3.1194i$ (4.0%)
42 Hz	$0.7350 - 2.8837i$	$0.2210 - 1.5083i$ (49.3%)	$0.7727 - 2.8127i$ (2.7%)
43 Hz	$0.6673 - 2.6902i$	$0.2926 - 1.4450i$ (46.9%)	$0.7973 - 2.5225i$ (7.7%)
44 Hz	$0.5653 - 2.3840i$	$0.1762 - 1.0256i$ (57.7%)	$0.8134 - 2.2329i$ (11.9%)

Table 7: The propagation constants of the negative going free waves for zone 3, identified from the measurements $\bar{\mu}_{n1}$, calculated from the preliminary FEM μ_{n1}, and calculated from the updated FEM $\mu^\star_{n1}$. The values between brackets indicate the relative error between the identified and the calculated propagation constants.

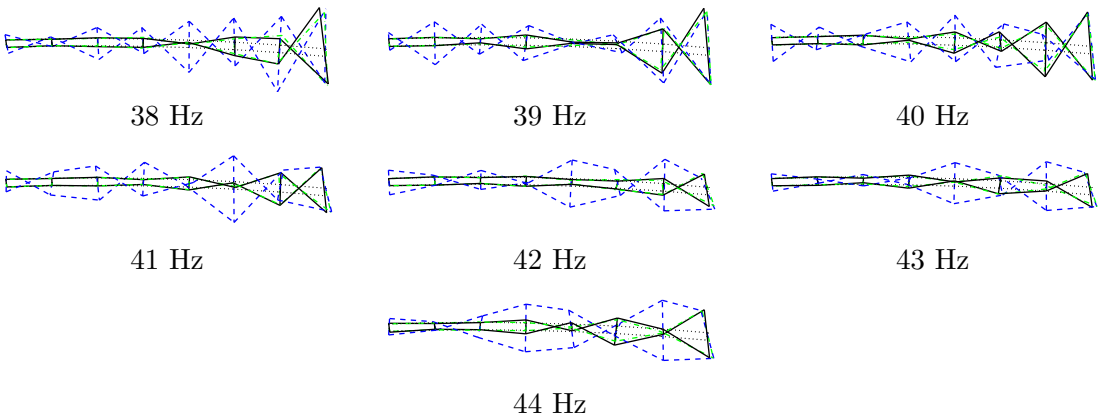

Fig. 20: Imaginary part of the negative going free waves identified from the measurements (solid black lines), calculated from the preliminary (dashed blue lines) and updated model (dot-dashed green lines), at frequencies 38 Hz to 44 Hz.

In order to assess the overall performance of the models obtained after updating, the identified FRFs for three measurement points in zone 3 indicated in Fig. 21 are compared to the FRFs obtained from the preliminary and updated FEM by application of the free wave superposition theory. The comparison is shown in Fig. 22. Only the vertical direction (z) is considered. The calculation of the FRFs from the FEM requires specific attention. The damping factors and the effective stiffness of the concrete deck in zones 2 and 3 have been updated based on the measured free wave characteristics, while the parameters of the other zones, which also intervene in the calculation of the FRFs, are not updated. It is assumed that the damping factor and the concrete stiffness of the deck in zone 1 are identical to the those obtained for zone 2 while those in zones 4 and 5 are identical to those obtained for zone 3. Furthermore, the influence of the passway in zone 4, which potentially affects the periodicity, is disregarded in the calculations. However, since the response is strongly attenuated after it passes through several units, as indicated in Section 4, it can be expected that the aforementioned modeling assumptions do not significantly affect the results. For the same reason, the expansion joints at the ends of the viaduct are not considered.

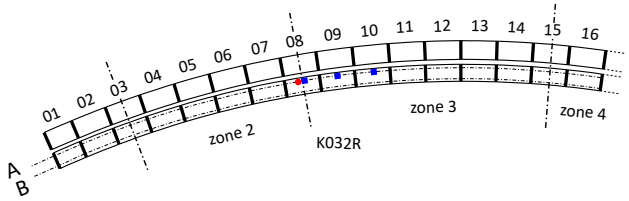

Fig. 21: The excitation location (solid red circle) and measurement locations (solid blue squares) considered for the validation of the model updating results.

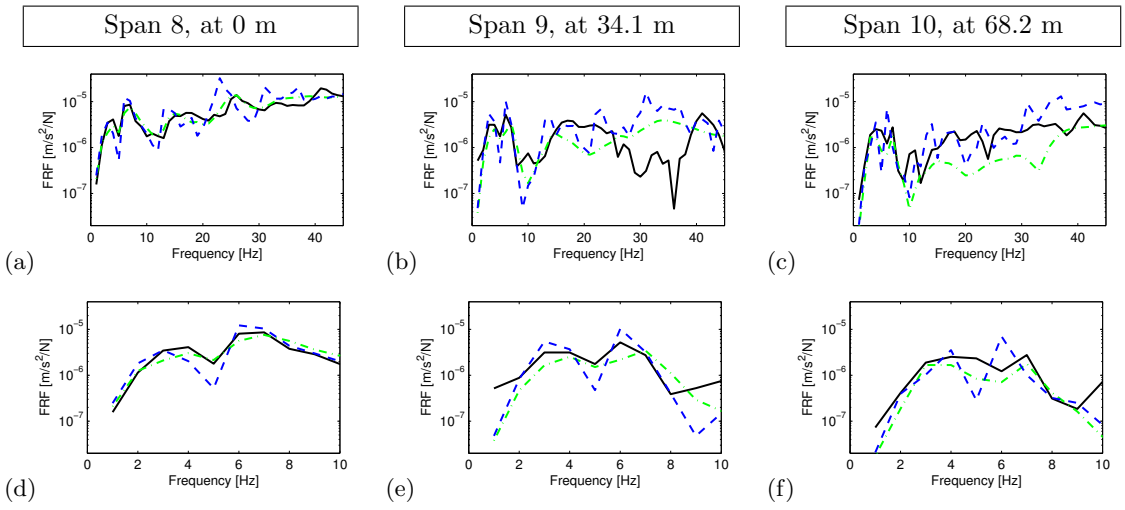

Fig. 22: Comparison of the identified and calculated FRFs corresponding to vertical excitation at span 8 and vertical acceleration measurements at span 8, 9, and 10 (solid black: identified from the measurements, dashed blue: calculated using the preliminary FEM, and dash-dotted green: calculated using the updated FEM). The top figures (a–c) show the frequency range between 0 Hz and 45 Hz. The bottom figures (d–f) show a zoom from 0 Hz to 10 Hz.

For the driving point measurement at span 8, it is observed that the model updating clearly improves the FRF prediction, as the calculated FRF obtained from the updated model is in very good agreement with the experimental one for the entire frequency range from 0 Hz to 45 Hz. For the remaining two points on spans 9 and 10, the improvement of the FRF prediction is less pronounced, with a relatively large discrepancy between the numerical and experimental FRFs, even after updating. It should be noted, however, that the updated model is generally more accurate in the low frequency range below 10 Hz. It is expected that a large part of the remaining modeling error is due to an incorrect model of the damping. In the present case, frequency-independent hysteretic damping is assumed. More complex damping models in combination with model updating may lead to an improved prediction capability of the FEM. This, however, requires a more extensive set of measurements to overcome ill-posedness in the model updating, and is therefore outside the scope of this paper.

Finally, another possible reason for the large mismatch in the frequency range above 10 Hz lies in the significant participation of the lateral waves in this frequency range (i.e. the third pair of spurious free waves shown in Figs. 12 and 13). These lateral waves are influenced by the column stiffness, which was not retained as an updating parameter. In the lower frequency range below 10 Hz, the bending of the deck composes the main contribution to the total response. As such, a more accurate prediction of the deck stiffness is expected to result in a better representation of the dynamic behavior in this low frequency range.

5.4. Discussion on the complementarity with conventional model updating

In addition to the presented model updating based on free wave characteristics, the authors have also performed a conventional model updating based on modal characteristics [20]. The modal characteristics have been obtained from a multi-setup modal identification. The identification resulted in 16 modes in the frequency range below 2 Hz, all corresponding to longitudinal and lateral motion of the bridge deck. As described in [21], several difficulties have been encountered in the modal identification of this viaduct. First, high model orders are required to obtain stable partial modes for each of the setups individually. This is due to the very large number of modes participating to the response in the frequency band of interest (0 – 2 Hz) and leads to time-consuming calculations, especially when compared to the free wave identification. Second, merging the partial modes obtained from the different setups requires exhaustive and proper user interaction. Finally, due to the high modal density, difficulties are encountered in pairing the experimental and computed modal characteristics in the model updating of the viaduct.

Compared to the modal identification, the free wave identification for the considered case is much easier to implement, the stable physical free waves are easier to pick up, and the procedure is much less time consuming. In addition, the matching of the calculated and identified free waves in the model updating is much easier compared to the mode matching in the case of the classical modal-based updating. Nonetheless, the free wave approach also has its limitations, which are worth mentioning. For example, as explained in the manuscript, a sufficient number of repetitive units needs to be measured to enable a sufficiently high model order in the free wave identification. On the other hand, if more units are measured, the response of the units far away from the excitation will inherently be more severely affected by ambient noise. This can be dealt with by providing an excitation with larger amplitude in the frequency band of interest, as to ensure an accurate estimation of the FRFs adopted in the free wave identification.

The results obtained from the conventional model updating cannot be directly compared to those obtained from the model updating based on free wave characteristics (1) due to the different frequency ranges considered in the modal identification (0 – 2 Hz) and the free wave identification (38 – 44 Hz) and (2) due to the difference in bridge motion contributing to the system response in both cases. In the case of the modal identification, the identification is based on the ambient response of the structure, primarily to wind loading, which mainly consists of longitudinal and lateral motion of the viaduct. The resulting modes mainly contain information on the foundation stiffness, the column stiffness, and the stiffness at the boundaries where the two viaducts are connected to each other and to their abutments. The deck stiffness, which is considered variable in the updating based on free wave characteristics, only affects the longitudinal and lateral modes to a minor extent. On the other hand, as evidenced from the sensitivity analysis in Section 5.2 of the revised manuscript, the identified free waves, which involve torsion and bending of the bridge deck, mainly contain information on the deck stiffness and the damping present in the system, while being insensitive to the column and foundation stiffness. As such, it can be concluded that the two approaches (based on modal characteristics and free wave characteristics) for the considered case provide complementary information, both in terms of frequency band and parameters that can be identified from the experiments.

6. Conclusions

This paper presents a validation of model updating based on free wave characteristics, using in situ measurements on a multi-span quasi-periodic viaduct in Bruges, Belgium. The free wave characteristics have been identified from FRF measurements on the bridge deck and are used to update a periodic model of the structure. It is found that the model updating leads to a much better prediction of the free wave characteristics, compared to the prediction obtained from an initial model based on the blueprints. Although less pronounced, it is also found that the model updating leads to a better prediction of the frequency response functions that describe the dynamic input-output behavior of the structure. Based on these results, it can be concluded that model updating based on free wave characteristics for the case of periodic or quasi-periodic structures is complementary to classical model updating based on modal characteristics.

Acknowledgments

The research presented in this paper has been performed within the framework of project OT/13/59 “Quantifying and reducing uncertainty in structural dynamics” and project C16/17/008 “Efficient methods for large-scale PDE-constrained optimization in the presence of uncertainty and complex technological constraints”, both funded by the Research Council of KU Leuven. The financial support of KU Leuven is gratefully acknowledged. Kristof Maes is a postdoctoral fellow of the Research Foundation Flanders (FWO), Belgium (grant No. 12Q9221N). The financial support by FWO is also gratefully acknowledged. Finally, the authors would also like to thank Jeffrey Depauw and Dieter Van Boeckel of the THV KW A11 for providing access to the viaduct and their support in the practical organization of the measurements.

References

[1] M. Friswell, J. Mottershead, Finite element model updating in structural dynamics, Kluwer Academic Publishers, Dordrecht, The Netherlands, 1995.

[2] C.-P. Fritzen, D. Jennewein, T. Kiefer, Damage detection based on model updating methods, Mechanical Systems and Signal Processing 12 (1) (1998) 163–186.

[3] E. Simoen, G. De Roeck, G. Lombaert, Dealing with uncertainty in model updating for damage assessment: A review, Mechanical Systems and Signal Processing 56–57 (2015) 123–149.

[4] J. Zhang, K. Maes, G. De Roeck, E. Reynders, C. Papadimitriou, G. Lombaert, Optimal sensor placement for multi-setup modal analysis of structures, Journal of Sound and Vibration 401 (2017) 214–232.

[5] J. Zhang, E. Reynders, G. De Roeck, G. Lombaert, Model updating of periodic structures based on free wave characteristics, Journal of Sound and Vibration 442 (2019) 281–307.

[6] D. Mead, Wave propagation in continuous periodic structures: research contributions from southampton, 1964 – 1995, Journal of Sound and Vibration 190 (3) (1996) 495–524.

[7] L. Brillouin, Wave propagation in periodic structures: electric filters and crystal lattices, MacGraw-Hill, New York, 1946.

[8] D. Mead, The forced vibration of one-dimensional multi-coupled periodic structures: An application to finite element analysis, Journal of Sound and Vibration 319 (2009) 282–304.

[9] L. Junyi, D. Balint, An inverse method to determine the dispersion curves of periodic structures based on wave superposition, Journal of Sound and Vibration 350 (2015) 41–72.

[10] D. Mead, A general theory of harmonic wave propagation in linear periodic systems with multiple coupling, Journal of Sound and Vibration 27 (2) (1973) 235–260.

[11] The MathWorks, MATLAB Optimization Toolbox User's Guide (2011).

[12] W. Heylen, S. Lammens, , P. Sas, Modal analysis theory and testing., Katholieke Universiteit Leuven, Leuven, Belgium, 1997.

[13] R. J. Allemang, The Modal Assurance Criterion – Twenty Years of Use and Abuse, Sound and Vibration Magazine (2003) 14–21.

[14] E. Reynders, System identification methods for (operational) modal analysis: review and comparison, Archives of Computational Methods in Engineering 19 (1) (2012) 51–124.

[15] ANSYS Inc., Basic Analysis Guide, ANSYS Release 11.0 (January 2007).

[16] S. François, M. Schevenels, D. Dooms, J. Jansen, J. Wambacq, G. Lombaert, G. Degrande, G. De Roeck, Stabil: an educational Matlab toolbox for static and dynamic structural analysis, Computer Applications in Engineering Education (2021). Accepted for publication.

[17] Stabil: a MATLAB toolbox for structural mechanics (version 3.0), https://bwk.kuleuven.be/bwm/stabil, accessed on 13/08/2020.

[18] American Petroleum Institute, Recommended practice for planning, designing and constructing fixed offshore platforms - working stress design, API recommended practice 2A-WSD (RP 2A-WSD) (2000).

[19] Databank ondergrond vlaanderen, `https://www.dov.vlaanderen.be/`, accessed 30/04/2018.

[20] J. Zhang, Numerical analysis and experimental assessment of the dynamic characteristics of periodic structures, Ph.D. thesis, Department of Civil Engineering, KU Leuven (2019).

[21] J. Zhang, K. Maes, G. De Roeck, G. Lombaert, Multi-setup operational modal testing of a multi-span viaduct, in: T. . Francis (Ed.), Proceedings of the 40th IABSE Symposium: Tomorrow's Megastructures, Nantes, France, 2018, pp. S6–37–S6–44.